Detecting permafrost active layer thickness change from nonlinear baseflow recession

M.G. Cooper[1], T. Zhou[1], K.E. Bennett[2], W.R. Bolton[3], E.T. Coon[4], S.W. Fleming[5,6,7], J.C. Rowland[2], and J. Schwenk[2]

[1]Atmospheric Sciences and Global Change Division, Pacific Northwest National Laboratory, Richland, WA, USA.

[2]Earth and Environmental Sciences Division, Los Alamos National Laboratory, Los Alamos, NM, USA.

[3]International Arctic Research Center, University of Alaska Fairbanks, Fairbanks, AK, USA.

[4]Climate Change Science Institute and Environmental Sciences Division, Oak Ridge National Laboratory, Oak Ridge, TN, USA.

[5]National Water and Climate Center, Natural Resources Conservation Service, US Department of Agriculture, Portland OR, USA.

[6]College of Earth, Ocean, and Atmospheric Sciences, and Water Resources Graduate Program, Oregon State University, Corvallis, OR, USA.

[7]Department of Earth, Ocean, and Atmospheric Science, University of British Columbia, BC, Canada.

Corresponding author: Matthew Cooper (matt.cooper@pnnl.gov)

Key Points:

- New relationships between active layer thickness and baseflow are developed for application to catchments underlain by permafrost.
- Theoretical predictions of active layer thickness trends agree with measured trends on the North Slope of Arctic Alaska.
- Novel methods are developed to estimate nonlinear recession flow parameters and related hydrologic signatures using generalized Pareto distributions.

Abstract

Permafrost underlies approximately one fifth of the global land area and affects ground stability, freshwater runoff, soil chemistry, and surface-atmosphere gas exchange. The depth of thawed ground overlying permafrost (active layer thickness, ALT) has broadly increased across the Arctic in recent decades, coincident with a period of increased streamflow, especially the lowest flows (baseflow). Mechanistic links between ALT and baseflow have recently been explored using linear reservoir theory, but most watersheds behave as nonlinear reservoirs. We derive theoretical nonlinear relationships between long-term average saturated soil thickness $\bar{\eta}$ (proxy for ALT) and long-term average baseflow. The theory is applied to 38 years of daily streamflow data for the Kuparuk River basin on the North Slope of Alaska. Between 1983–2020, the theory predicts $\bar{\eta}$ increased 0.11 ± 0.17 [2σ] cm a^{-1}, or 4.4 ± 6.6 cm total. The rate of change nearly doubled to 0.20 ± 0.24 cm a^{-1} between 1990–2020, during which time field measurements from CALM (Circumpolar Active Layer Monitoring) sites in the Kuparuk indicate ALT increased 0.31 ± 0.22 cm a^{-1}. The predicted rate of change more than doubled again between 2002–2020, mirroring a near doubling of observed ALT rate of change. The inferred increase in $\bar{\eta}$ is corroborated by GRACE (Gravity Recovery and Climate Experiment) satellite gravimetry, which indicates that terrestrial water storage increased ~0.80 ± 3.40 cm a^{-1}, ~56% higher than the predicted increase in $\bar{\eta}$. Overall, hydrologic change is accelerating in the Kuparuk River basin, and we provide a theoretical framework for estimating changes in active layer water storage from streamflow measurements alone.

Plain Language Summary

Streamflow has increased in most areas of the Arctic in recent decades. This increase in streamflow has occurred along with a period of rising air temperatures and thawing permafrost. Permafrost is typically overlain by a layer of seasonally unfrozen ground referred to as the active layer, which gets deeper as permafrost thaws. As the active layer deepens, it can store more water. Water may also take more time to flow through a thicker active layer than it would atop frozen ground. Because there is more space to store water, thicker active layers leads to increased soil water storage which sustains streamflow during dry periods and enhances overall increased streamflow and subsurface flow. We developed an approach to measure how quickly the active layer thickness is changing using the rate of change of streamflow. This is useful because streamflow measurements are widely available and easy to obtain, whereas active layer thickness measurements are difficult to measure and therefore uncommon. If the equations we developed accurately predict measured values, the pace at which active layer thickness changes can be estimated from streamflow measurements, which would expand the current knowledge of permafrost thaw rates and provide an independent way to validate simulations of active layer thickness.

1 Introduction

Permafrost underlies approximately one fifth of the global land area and is an important control on slope stability, shoreline erosion, water available for runoff, soil biogeochemistry, and gas exchange between the land surface and atmosphere (McKenzie et al., 2021; Walvoord & Kurylyk, 2016). The layer of seasonally-thawed ground overlying permafrost known as active layer is a sensitive indicator of permafrost response to climate change (Kurylyk et al., 2014). In recent decades, active layer thickness (ALT) has increased at high latitude observation sites, concurrent with observed increases in streamflow, especially the lowest flows (hereafter referred to as *baseflow*) (Duan et al., 2017; Rennermalm et al., 2010; Smith et al., 2007).

The trends in ALT and baseflow are thought to be linked via: 1) increased soil water storage capacity within a thicker active layer, 2) increased soil water residence time as flow paths lengthen within a more continuous active layer, and 3) direct contribution of thaw water to streamflow, each of which may support higher baseflow in high latitude rivers (Figure 1) (Brutsaert & Hiyama, 2012; Evans et al., 2020; Jacques & Sauchyn, 2009; Lyon & Destouni, 2010; Walvoord et al., 2012; Walvoord & Striegl, 2007). In addition, heat transport via lateral subsurface flow within the active layer enhances permafrost thaw (Rowland et al., 2011; Sjöberg et al., 2021), suggesting a positive feedback. Changes in the water balance driven by precipitation and evaporation are also thought to have contributed to a broad-scale increase in freshwater runoff delivered to the Arctic Ocean in recent decades (Feng et al., 2021).

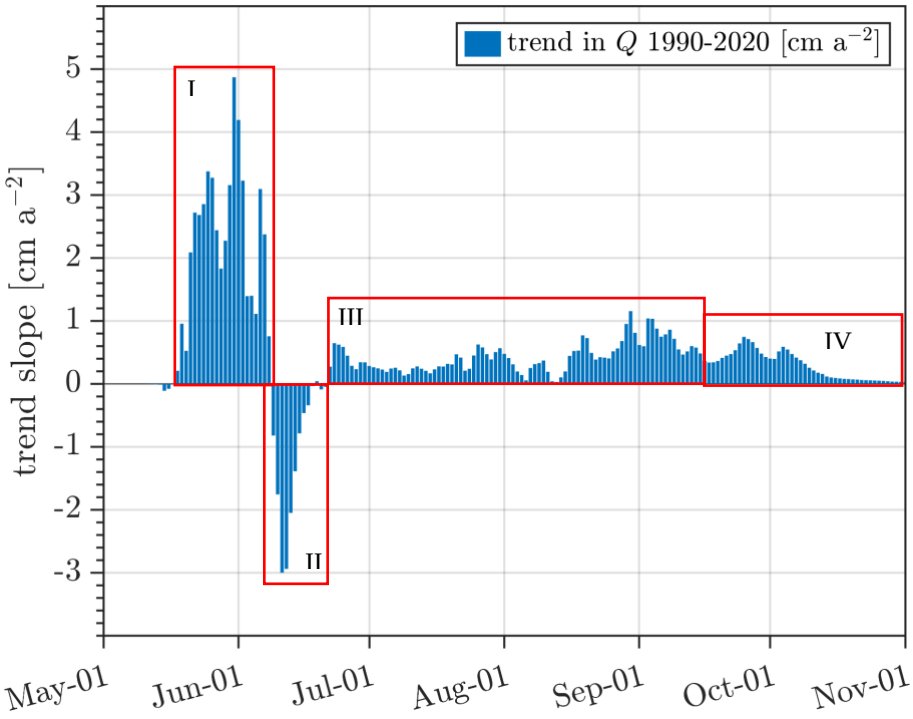

Figure 1: Trend in daily streamflow for each day from 15 May to 1 December for the Kuparuk River on the North Slope of Arctic Alaska. Four conceptual periods are highlighted by red box with hypothetical explanations: I) higher May–June flows driven by earlier snowmelt, II) lower June flows driven by snowmelt deficit, III) higher June–September flows driven by increased precipitation, and IV) higher September–December flows driven by increased baseflow. The approximately smooth increase followed by smooth recession of the daily trend magnitudes during period IV supports the idea that permafrost thaw and increased catchment storage are supplying additional water to baseflow, rather than a process such as precipitation that might resemble the quasi-random structure of period III. River discharge data are provided by United States Geological Survey (gage 1596000).

One approach to analyzing mechanistic links between ALT change and streamflow change is baseflow recession analysis (Brutsaert & Hiyama, 2012; Evans et al., 2020), which is a classical method in hydrology that relates groundwater storage S to recession flow Q with a power function relationship: $Q = c(S - S_c)^{1/\beta}$, where S_c is a critical storage below which the relationship does not hold, c is a scale parameter related to aquifer properties via hydraulic groundwater theory, and β is an order parameter indicating the degree of nonlinearity in the storage-discharge relationship. For the special case of a linear reservoir ($\beta = 1$), simple relationships between long-term change in ALT and long-term change in Q can be derived under the assumption that S is primarily a function of water storage in active layer, that is, the saturated ALT (Brutsaert & Hiyama, 2012).

If these simple relationships are applicable to real-world catchments, it suggests ALT trends can be diagnosed from streamflow measurements alone. However, streamflow recession in real-world catchments is typically not consistent with linear reservoir theory, meaning real-world recession data suggest $\beta \neq 1$ (Aksoy & Wittenberg, 2011; Jachens et al., 2020). Although nonlinear reservoir behavior is well-documented and widely explored in the hydrologic science literature, to our knowledge, the theoretical relationship between saturated ALT change and baseflow has not been generalized to the nonlinear case (Hinzman et al., 2020; Sergeant et al., 2021). Doing so could open the door to retrospective analysis of ALT change at broad scales and is necessary before such methods can be applied beyond the special case of linear reservoir theory. Exploring the nonlinear case also merits attention because the parameter β can be related to aquifer properties (Rupp & Selker, 2006b), which adds another dimension along which ALT can be related to streamflow, which is more widely observed than ALT.

The aim of this paper is to generalize the hydraulic groundwater theory of streamflow sensitivity to saturated ALT change to the case of nonlinear storage-discharge behavior. Section 2 describes the background to the theory. In Section 3, we extend an earlier theory (Brutsaert & Hiyama, 2012) of saturated ALT change for flat catchments with homogeneous soils and linear storage-discharge behavior to the case of sloped catchments with non-homogeneous soils and nonlinear storage-discharge behavior. The non-homogeneity considered here is vertical variation in saturated lateral hydraulic conductivity (Rupp & Selker, 2006b). These three characteristics are consistent with real-world catchment behavior, although we emphasize the theory remains an effective one based on hillslope-scale behavior. The main theoretical result is a set of new equations (Section 3) that relate long-term average saturated ALT change to long-term baseflow change. In Section 4 we describe a baseflow recession algorithm that implements the theory and in Section 5 we apply it to 38 years of daily streamflow and 30 years of annual ALT measured in the Kuparuk River basin on the North Slope of Alaska (Figure 2). Section 6 compares predictions to observations. The paper concludes with a discussion of methodological limitations, which include high sensitivity to accurate knowledge of soil properties, and the dependence on large-sample streamflow data to estimate power-law scaling of recession flows.

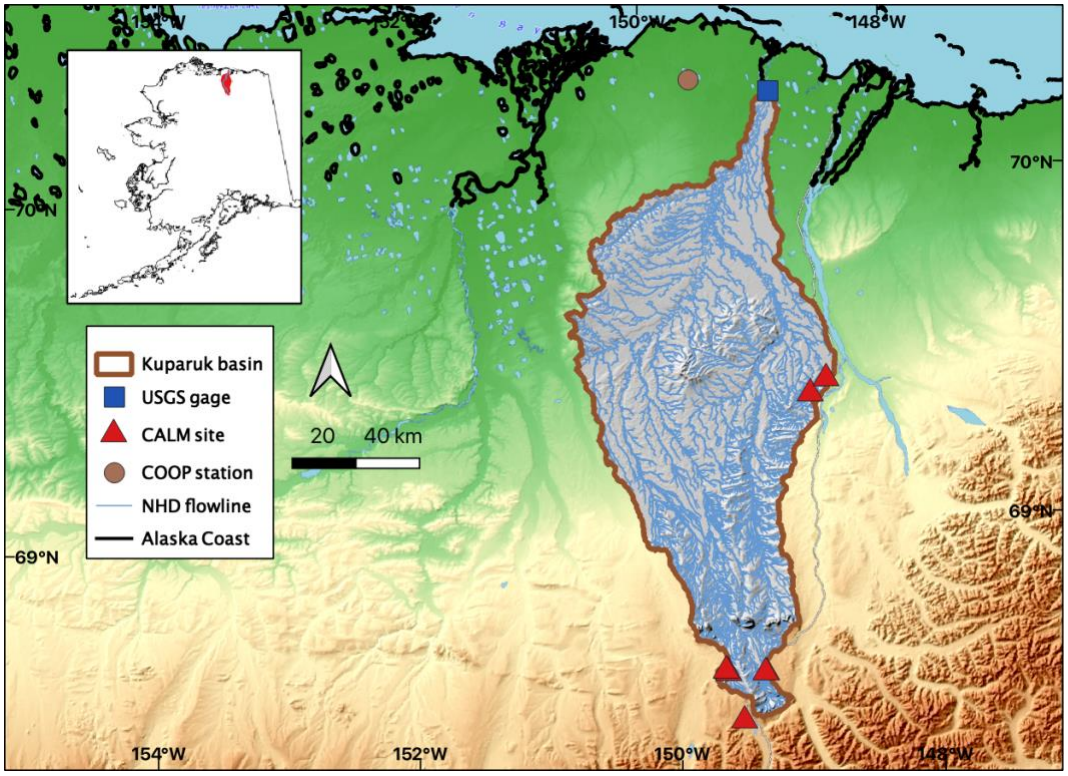

Figure 2: Study area map showing Kuparuk basin outline, locations of United States Geological Survey (USGS) gage 1596000, Circumpolar Active Layer Monitoring network sites, and United States National Oceanic and Atmospheric Administration Cooperative Observer Program weather station 505136. Kuparuk basin topography is from USGS interferometric synthetic aperture radar 5 m resolution digital terrain model. Basemap credit: ©OpenTopoMap (CC-BY-SA).

2 Hydraulic groundwater theory

2.1 Storage-discharge relationship

Baseflow recession analysis relates groundwater storage S to baseflow Q with a single-valued catchment-scale storage-discharge relationship:

$$Q = c(S - S_c)^{1/\beta}, \qquad \beta \neq 0 \tag{1}$$

where baseflow Q has dimensions L/T, scale parameter c has dimensions $L^{(b-1)/(b-2)}/T$, order parameter β is dimensionless, and $S_c = S(Q \to Q_{min})$ is a critical storage below which (1) does not hold.

During periods when precipitation, evaporation, and any other factor that affects catchment water storage is negligible relative to streamflow, the rate of change of catchment water storage can be approximated by the conservation equation:

$$\frac{\mathrm{d}S}{\mathrm{d}t} = -Q, \qquad (P - E \cong 0) \tag{2}$$

where S has dimension L and represents water stored in upstream catchment aquifers available to supply Q. With (1) and (2), the rate of change of Q can be expressed as a power function of Q:

$$-\frac{\mathrm{d}Q}{\mathrm{d}t} = aQ^b \tag{3}$$

where parameter a has dimensions $T^{(b-2)}/L^{(b-1)}$, b is dimensionless, and the parameters in (1) and (3) are related as $c = (a\beta)^{1/\beta}$ and $\beta = 2 - b$.

At hillslope scales, (1) and (3) acquire physical meaning from solutions to the one-dimensional (1-D) lateral groundwater flow equation:

$$\frac{\partial h}{\partial t} = \frac{k_D}{\phi}\frac{D^{-n}}{(n+1)}\frac{\partial}{\partial x}\left[h^{n+1}\left(\frac{\partial h}{\partial x}\cos\theta + \sin\theta\right)\right] + \frac{I}{\phi} \tag{4}$$

where $h(x,t)$ is the phreatic water surface along horizontal dimension x, ϕ is drainable porosity, D is aquifer thickness, n is a constant, θ is bed slope, I is recharge rate, and:

$$k(z) = k_D(z/D)^n, \tag{5}$$

is lateral saturated hydraulic conductivity along vertical dimension z with $k_D = k(D)$. Various approximate and exact solutions to (4) for an unconfined aquifer draining to a fully- or partially-penetrating channel can be written in the same form as (3) (Appendix A) (Brutsaert & Nieber, 1977; van de Giesen et al., 2005; Rupp & Selker, 2006b). At catchment scales, a and b can be interpreted as lumped parameters linked to catchment-effective drainage density and aquifer transmissivity, porosity, slope, and breadth (distance along the land surface from channel to catchment divide) (Brutsaert, 2005). In the linear case ($b = 1 \leftrightarrow n = 0$), the solution to (3) is an exponential $Q \sim \mathrm{e}^{-at}$ with decay constant a (Boussinesq, 1903). For $b > 1$, the solution to (3) is a power function $Q \sim t^{-\alpha}$ with $\alpha = 1/(b-1)$ (Section 2.3).

2.2 Drainable porosity and the effective water table

The groundwater stored in a catchment can be defined in terms of a thickness of liquid water stored in an effective catchment aquifer (Brutsaert & Hiyama, 2012):

$$(S - S_\mathrm{r}) = \phi\eta \tag{6}$$

where η is an effective water table thickness $[L]$ relative to an arbitrary reference S_r. In this study, we assume $S_\mathrm{c} = S_\mathrm{r}$. In general, $S_\mathrm{c} \neq 0$ but it's absolute magnitude has no bearing on the following analysis (Kirchner, 2009).

In this study and in the general context of hydraulic groundwater theory, the active groundwater layer is treated as a Boussinesq aquifer. Under the Dupuit-Forchheimer assumption for an unconfined aquifer, vertical fluxes are assumed negligible relative to horizontal fluxes and the water table is treated as a free surface, implying capillarity is also neglected (Brutsaert, 2005). The effect of capillarity on storage change can be parameterized in terms of ϕ, defined as the change in storage per unit area per unit change in effective water table (Brutsaert, 2005):

$$\phi = \frac{\partial S}{\partial \eta} = \frac{1}{\mathrm{d}\eta/\mathrm{d}D}\frac{\partial S}{\partial D}, \qquad 0 < \phi < 1, \tag{7}$$

where η is a quasi-steady ("average") groundwater layer thickness. Equation (7) extends the usual form $\phi = \partial S/\,\partial \eta$ to a timescale over which D is changing and assumes $\mathrm{d}\eta/\mathrm{d}D$ is a linear function of D over the timescale and soil thickness represented by $(\mathrm{d}\eta/\mathrm{d}D)\Delta D$. It does not assume a functional form for ϕ during recession, but such assumptions are made in Section 4.

2.3 Characteristic timescales

With (2) and (3), a storage sensitivity function can be defined:

$$\frac{\mathrm{d}S}{\mathrm{d}Q} = \tau(Q), \tag{8}$$

where:

$$\tau(Q) = a^{-1}Q^{1-b} \tag{9}$$

is a nonlinear drainage timescale that carries the dimension of $\mathrm{d}t$ in (3). Note that $\tau^{-1}(Q) = \mathrm{d}Q/\mathrm{d}S$ is denoted $g(Q)$ elsewhere (Berghuijs et al., 2016; Kirchner, 2009).

Integration of (3) over some time interval $t - t_0$, with $t_0 = 0$ gives:

$$Q(t) = [Q_0^{1-b} + a(b-1)t]^{\frac{1}{1-b}} \tag{10}$$

and integration of (8) gives a mathematically identical form parameterized by $S(t)$:

$$Q(t) = [a(2-b)(S - S_\mathrm{r})]^{\frac{1}{2-b}} \tag{11}$$

thereby recovering (1).

Although τ has dimension time, (9) implies non-characteristic time scaling, since τ is a function of Q. However, we can estimate an expected value $\langle\tau\rangle$ from the probability density transform of (10). Evaluating $\int_{Q_0}^{0} \mathrm{d}\tau\ C \cdot Q(\tau) = 1$, where $Q(\tau) = Q_0(\tau/\tau_0)^{1/(1-b)}$ and C normalizes the integral if $1 < b < 2$, we find:

$$p(\tau) = \left(\frac{2-b}{b-1}\right)\left(\frac{1}{\tau_0}\right)\left(1 + \frac{\tau - \tau_0}{\tau_0}\right)^{\frac{1}{1-b}}, \qquad \tau_0 \le \tau \; and \; 1 < b < 2 \tag{12}$$

which is a generalized Pareto (GP) distribution with shape parameter $\zeta = (b-1)/(2-b)$, scale parameter $\sigma = \tau_0(b-1)/(2-b)$, and threshold parameter $\mu = \tau_0$. In this case $\mu = \sigma/\zeta$ and therefore (10) is equivalent to an unbounded Pareto distribution: $p(\tau) = (\alpha - 1)/\tau_0(\tau/\tau_0)^{-\alpha}$, with shape parameter $\alpha = 1/(b-1)$ and scale parameter τ_0.

A general feature of a power law such as (12) is that the process it describes lacks a characteristic timescale for $1 < b$. Moreover, if $3/2 \le b$, $\langle\tau\rangle \to +\infty$ for $0 < Q_0$, where $\langle\tau\rangle = \int \mathrm{d}\tau\ \tau \cdot p(\tau)$. For $1 < b \le 3/2$, however:

$$\langle\tau\rangle = \tau_0\left(\frac{2-b}{3-2b}\right), \qquad \langle Q\rangle = Q_0\left(\frac{2-b}{3-b}\right), \qquad \langle t\rangle = \tau_0\left(\frac{1}{3-2b}\right) \tag{13}$$

where $\langle\tau\rangle$ is an expected drainage timescale, $\langle Q\rangle$ is an expected value of baseflow, and $\langle t\rangle$ is an expected duration of baseflow. Note $\langle Q\rangle$ remains finite for $1 < b < 2$.

As implied by (12), a critical threshold exists at $b = 2$, above which (10) is not normalizable. In the context of (4), $b = 2$ marks a transition from small-t ("early-time") to large-t ("late-time") drainage, where theoretical and numerical solutions indicate $b = 3$ (but can approach $+\infty$) during early-time and $1 < b < 2$ during late-time, separated by an "intermediate" period (van de Giesen et al., 2005; Rupp & Selker, 2006b).

In general, (11) will be used to derive expressions relating ALT to baseflow, with (12) and (13) providing a method to estimate $\langle\tau\rangle$ and $\langle Q\rangle$, and the basis for a discussion of the important dependence on τ_0.

3 New equations for change in permafrost active groundwater layer thickness from nonlinear baseflow recession analysis

We first rewrite (11) with a and S parameterized by D (dependence on time is omitted for clarity):

$$\bar{Q} = \left[a(D)(2-b)(\overline{S(D)} - S_{\mathrm{r}})\right]^{\frac{1}{2-b}} \tag{14}$$

where overbars indicate temporal averages over a period comparable to $\langle t \rangle$. The total derivative of (14) in this case is:

$$\frac{\mathrm{d}\bar{Q}}{\mathrm{d}t} = \frac{\partial \bar{Q}}{\partial t} + \left(\overline{\frac{\partial Q}{\partial S}}\,\overline{\frac{\partial S}{\partial D}} + \overline{\frac{\partial Q}{\partial a}}\,\frac{\partial a}{\partial D}\right)\frac{\mathrm{d}D}{\mathrm{d}t} \tag{15}$$

where $\partial S / \partial D$ is defined in (7). Strictly speaking, D represents the initial saturated aquifer thickness when $Q = Q_0$, and η is the average saturated aquifer thickness over a period comparable to $\langle t \rangle$. As in prior studies (Brutsaert & Hiyama, 2012; Lyon et al., 2009), D is treated as proxy for ALT and $\bar{\eta}$ as proxy for its average value, and hereafter we use them interchangeably in the context of (15).

Given (6), (9) and (14), (15) can be written:

$$\frac{\mathrm{d}\bar{Q}}{\mathrm{d}t} = \frac{\partial \bar{Q}}{\partial t} + \frac{\phi}{\tau}\left(1 + \frac{D}{a}\frac{\partial a}{\partial D}\right)\frac{\mathrm{d}\bar{\eta}}{\mathrm{d}t}. \tag{16}$$

A general result of hydraulic groundwater theory is that a can be expressed as a power function of D: $a \propto D^N$, where N is a constant function of b and can be related to $k(z)$ (Appendix A). For the present case, we reviewed 19 different solutions to (4) collated in Figure 2 and Figure 3 of Rupp and Selker (2006b) (hereafter RS06). Setting aside two kinematic-wave solutions (Beven, 1982), we found for the 17 remaining solutions a can be written as:

$$a(D) = c_1 D^N (1 + c_2 D^M) \tag{17}$$

where c_1 and c_2 are constants that depend on the particular solution. For all six horizontal-aquifer solutions and six sloped-aquifer solutions, $c_2 = 0$. Five sloped-aquifer solutions having $c_2 \neq 0$ effectively treat $a(D)$ as the horizontal equivalent multiplied by a dimensionless slope factor $\nu = B/D \tan\theta$. In these cases, if ν is treated as a constant parameter, $c_2 D^M$ is constant, and (17) satisfies the following general property of a power function:

$$\frac{\partial a}{\partial D} = N\frac{a}{D} \tag{18}$$

which when combined with (16) to evaluate (15) yields:

$$\frac{\mathrm{d}\bar{Q}}{\mathrm{d}t} \cong \frac{\phi}{\tau}(1+N)\frac{\mathrm{d}\bar{\eta}}{\mathrm{d}t} \tag{19}$$

where $\partial\bar{Q}/\partial t = 0$ for clarity. In this case, (19) can be rearranged and linearized around a reference τ to express $\mathrm{d}\bar{\eta}/\mathrm{d}t$ in terms of $\mathrm{d}\bar{Q}/\mathrm{d}t$:

$$\frac{\mathrm{d}\bar{\eta}}{\mathrm{d}t} = \frac{\tau_\mathrm{r}}{\phi}\left(\frac{1}{N+1}\right)\frac{\mathrm{d}\bar{Q}}{\mathrm{d}t} \tag{20}$$

where τ_r is a reference τ taken at a reference time, or as an average value over a reference period, and $\lambda = \tau_\mathrm{r}/\phi[1/(N+1)]$ is a (linearized) sensitivity coefficient.

As an alternative to (15), the long-term change in active layer thickness can be expressed in terms of the direct dependence between a and D:

$$\frac{\mathrm{d}a}{\mathrm{d}t} = \frac{\mathrm{d}a}{\mathrm{d}D}\frac{\mathrm{d}D}{\mathrm{d}t}. \tag{21}$$

Rearranging in terms of D and substituting (18) yields, upon linearization:

$$\frac{\mathrm{d}\bar{\eta}}{\mathrm{d}t} = \frac{\eta_\mathrm{r}}{a_\mathrm{r}}\left(\frac{1}{N}\right)\frac{\mathrm{d}a}{\mathrm{d}t} \tag{22}$$

where η_r and a_r are reference values as previously described.

Noting that $N = 3 - 2b$ for all but two sloped-aquifer solutions (Rupp & Selker, 2006b), we can write particular forms of (20) and (22):

$$\frac{\mathrm{d}\bar{\eta}}{\mathrm{d}t} = \frac{\tau}{\phi}\left(\frac{1}{4-2b}\right)\frac{\mathrm{d}\bar{Q}}{\mathrm{d}t} \tag{23}$$

and:

$$\frac{\mathrm{d}\bar{\eta}}{\mathrm{d}t} = \frac{\eta}{a}\left(\frac{1}{3-2b}\right)\frac{\mathrm{d}a}{\mathrm{d}t} \tag{24}$$

which recover Equation 10 and Equation 13 of Brutsaert and Hiyama (2012) for the linear case $b = 1$.

In (24), ϕ is contained within the definition of a, which is an advantage because ϕ is highly uncertain (Lv et al., 2021). However, (24) requires a value for η_r, which may be unavailable (Brutsaert & Hiyama, 2012). In addition, (24) requires a reliable estimate of $\mathrm{d}a/\mathrm{d}t$, which can be difficult to obtain relative to $\mathrm{d}\bar{Q}/\mathrm{d}t$, because a is not observed.

4 Baseflow recession analysis

Methods to estimate drainage timescale τ, recession parameters a and b, and drainable porosity ϕ are required before (20) can be applied to data. We designed a baseflow recession analysis algorithm for this purpose (Figure 3). The algorithm detects periods of declining flow (recession events) on quality-controlled streamflow timeseries, approximates $\mathrm{d}Q/\mathrm{d}t$, and fits (3) to estimate a and b. Event detection follows recommendations in Dralle et al. (2017), $\mathrm{d}Q/\mathrm{d}t$ is estimated with an exponential time step (Roques et al., 2017), and nonlinear least-squares minimization is used to fit (3). In addition to the recommendations in Dralle et al. (2017), we exclude recession flows on days with recorded rainfall if $\mathrm{d}Q/\mathrm{d}t$ attains a local maximum within a six-day window centered on the date of rainfall, that is, if a rainfall response is detected (Figure 3b). The event-based a, b, and Q values are then used to compute $\tau(Q)$ for each event from (9), yielding a sample τ population of size equal to the sample size of Q. Methods to estimate expected values of τ, b, and ϕ are described in the following two sections.

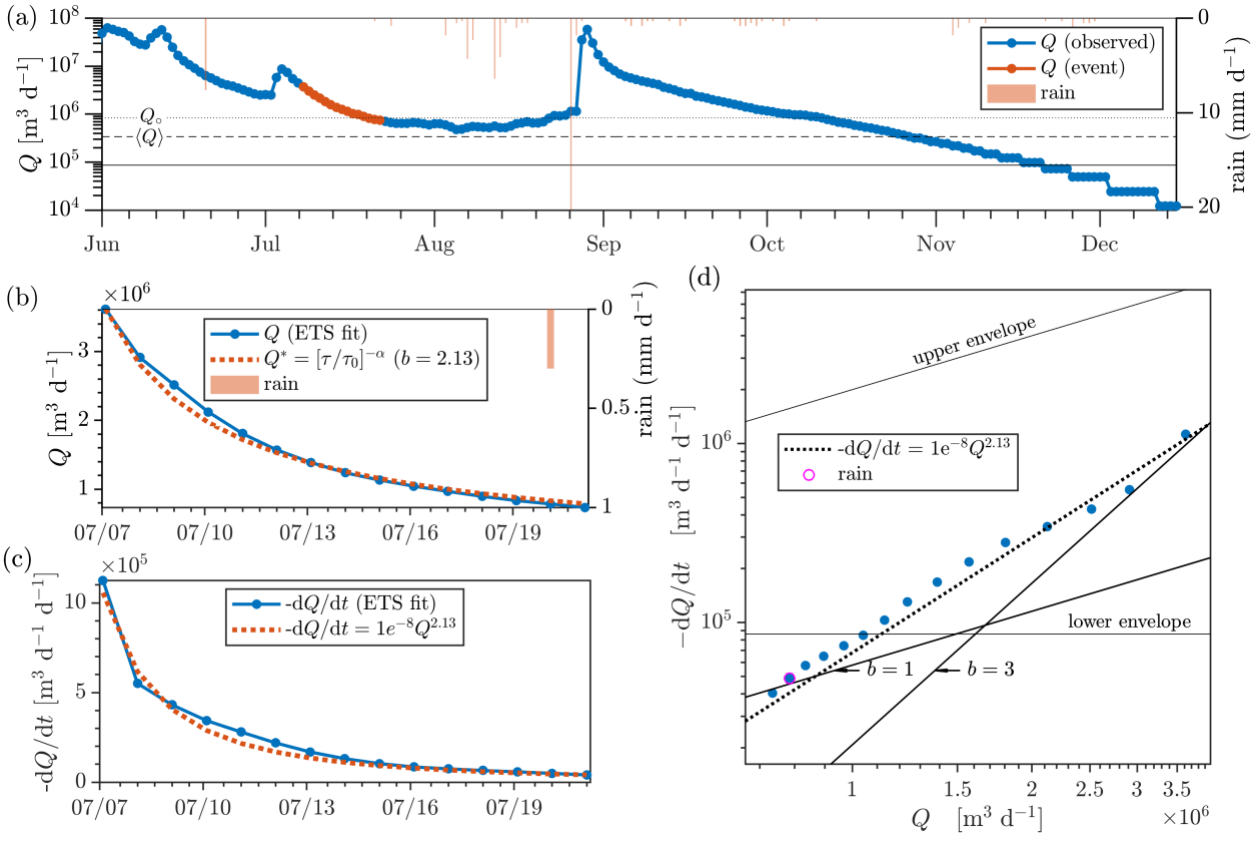

Figure 3: Example application of baseflow recession algorithm: **(a)** daily streamflow Q during 1992 and one highlighted recession event on a logarithmic scale against time (left axis), and rainfall (vertical bars) on a linear scale (right axis). Horizontal lines are Q_0 (dotted), $\langle Q \rangle$ (dashed), and minimum observable $-\mathrm{d}Q/\mathrm{d}t$ (solid) dictated by the streamflow precision (Rupp & Selker, 2006a) (value shown is 1 m^3 s^{-1} d^{-1}; actual precision varies). **(b-c)** Estimated Q and $-\mathrm{d}Q/\mathrm{d}t$ computed with an exponential time step (ETS) (Roques et al., 2017) compared to predictions from Equation (10) and Equation (3) using best-fit parameters a and b. **(d)** Point-cloud diagram with non-linear least squares fit to Equation (3), rainfall (open circles), and four reference lines: the "upper-envelope" (line of slope $b = 1$ and intercept $a = 2$) represents the maximum $-\mathrm{d}Q/\mathrm{d}t$ for given Q dictated by the daily timestep (Rupp & Selker, 2006a), "lower-envelope" (horizontal line) represents the minimum observable $-\mathrm{d}Q/\mathrm{d}t$ (~86400 m^3 d^{-1} d^{-1}), line of slope $b = 1$ passing through the 5th percentile of $-\mathrm{d}Q/\mathrm{d}t$ represents the theoretical late-time fit, and a line of slope $b = 3$ passing through the 95th percentile of $-\mathrm{d}Q/\mathrm{d}t$ represents the theoretical early-time fit. The permissive rainfall filter retains streamflow unless rainfall exceeds 1 mm d^{-1} and $-\mathrm{d}Q/\mathrm{d}t$ attains a local maximum within a three-day window.

4.1 Estimating drainage timescale τ and recession parameters a and b

As described in Section 2.2, the probability density function $p(\tau)$ follows a Pareto distribution, unlike $p(Q)$ which can be shown to follow the q-exponential distribution of non-extensive statistical mechanics (Tsallis, 1988). Both distributions are associated with power law scaling. An advantage of the Pareto transformation over the q-exponential is that widely-used and thoroughly vetted algorithms are available to fit the distribution, including the

lower-bound τ_0 (Clauset et al., 2009; Hanel et al., 2017). In particular, an expression for the maximum likelihood estimate of $\hat{\alpha}$ exists in closed form. This means $\hat{\tau}_0$ can be found by a global search over all $\tau_0 \in \tau$ for the value that minimizes a measure of distance between the data and Pareto distribution fit to $\tau \geq \tau_0$. We applied a widely-used algorithm that minimizes the Kolmogorov-Smirnoff distance to estimate $\hat{\tau}_0$ (Clauset et al., 2009).

The Pareto distribution fit to $p(\tau)$ also provides an unbiased estimate of $\hat{b}$ via the relationship:

$$b = 1 + 1/\alpha, \tag{25}$$

see (10)–(13). Equation 25 provides a method to estimate b in lieu of ordinary least-squares fitting to a bi-logarithmic plot of Q versus $-\mathrm{d}Q/\mathrm{d}t$ (i.e., the "point cloud"). In contrast, the parameter a is not provided by this procedure. Although we only require a at the scale of individual recession events to estimate $\tau(Q)$, it is useful to have a global estimate, call it $\hat{a}$, to maintain analytical consistency with $\hat{b}$ and $\hat{\tau}_0$ when estimating quantities such as ϕ (Section 4.2). We estimated $\hat{a}$ by constraining a line of slope $\hat{b}$ to pass through the centroid of the $\tau \geq \hat{\tau}_0$ point cloud. This procedure is illustrated graphically in Section 5, where analogous procedures are used to estimate $\hat{Q}_0$ and $\langle Q \rangle$, but can be defined mathematically as: $\hat{a} = \overline{\log[-\mathrm{d}Q/\mathrm{d}t]} - \hat{b}\,\overline{\log[Q]}$, where overbars indicate geometric averages of the respective quantities within the sample space $\tau \geq \hat{\tau}_0$.

In practice, once $\hat{\tau}_0$ was determined, the Pareto fit was repeated 1000 times by bootstrap resampling with replacement from the underlying $\tau \geq \hat{\tau}_0$ sample. Reported parameters are averages of the bootstrapped parameter ensemble. Uncertainties are presented as 95% confidence intervals (~two standard deviations).

4.2 Estimating drainable porosity ϕ

Estimates of ϕ were obtained from a method proposed by Brutsaert and Nieber (1977). In this approach, an early-time expression for a is substituted into a late-time solution and common terms are eliminated, leaving ϕ as the sole unknown. Taking the early-time solution ($b = 3$) from Polubarinova-Kochina (1962) and the linearized late-time solution ($b = 1$) from Boussinesq (1903), we find:

$$\phi = \frac{1}{DA}\left(\frac{c_1}{a_1}\right)^{1/2}\left(\frac{c_2}{a_2}\right)^{1/2}, \tag{26}$$

where DA is an effective aquifer volume, a_1 and a_2 are the respective early- and late-time estimates of a, $c_1 = 1.133$, and $c_2 = \pi^2 p$, where $0 < p \leq 1$ linearizes the water table variation during aquifer drawdown and in the context of (26) is assigned a value $p = 1/3$ (Brutsaert & Nieber, 1977). Using the nonlinear late-time solution ($b = 3/2$) from Boussinesq (1904), we find:

$$\phi = \frac{1}{DA}\left(\frac{c_1}{a_1}\right)^{1/3}\left(\frac{c_2}{a_2}\right)^{2/3}, \tag{27}$$

where again $c_1 = 1.133$ and $c_2 = 4.804$. The same approach with the nonlinear early- and late-time solutions for a power-function $k(z)$ profile (Rupp & Selker, 2005) (hereafter RS05) yields:

$$\phi = \frac{1}{DA}\left(\frac{c_1}{a_1}\right)^{\frac{1}{n+3}}\left(\frac{c_2}{a_2}\right)^{\frac{1}{n+3}}, \tag{28}$$

where:

$$c_1 = f_{R1}, \qquad c_2 = \frac{(f_{R2})^{n+2}}{2^n(n+1)}, \qquad -1 < n \tag{29}$$

and f_{R1} and f_{R2} are parameters related to the Beta function evaluated at $n + 2$ and 2, and $(n + 2)/(n + 3)$ and $1/2$, as defined by Equation 26 and Equation 49 of RS05, respectively.

Although the late-time RS05 solution for a power-function $k(z)$ profile was derived under the assumption $0 \leq n$, the solution appears valid on $-1 < n$, where b ranges from 1 to 2 as n varies from -1 to $+\infty$ (and $a \to +\infty$ at $n = -1$). However, values of $-1 < n < 0$ predict an inverted $k(z)$ profile given (5). One benefit of (28), therefore, is its compatibility with any late-time value $3/2 \leq b < 2$, or with $1 < b < 2$ if an inverted $k(z)$ profile is acceptable, whereas (26) and (27) assume late-time $b = 1$ and $b = 3/2$, respectively.

We tested two methods to estimate a_1 and a_2 for application of (26)–(28). In the first method, a line of slope $b = 3$ was fit through the 95th percentile of the Q point-cloud to approximate early-time a_1, and lines of slope $b = 1$, $b = 3/2$, and $\hat{b}$ were fit through the $\tau \geq \hat{\tau}_0$

point cloud to approximate late-time a_2. For the latter estimate, $a_2 = \hat{a}$ as described in Section 4.1. The second method was similar to the first, except that a_1 and a_2 were fit to each individual event rather than the point cloud. This resulted in a sample of ϕ values to which we fit a Beta distribution, which is appropriate for random variables defined on $(0,1)$. Reference values for catchment area $A = 8400$ km^2, drainage network length $L = 320$ km, active layer thickness $D = 0.5$ m, and slope $\theta = 1.15^{\circ}$ were used in each case, where θ was chosen to be consistent with the mean catchment elevation (~265 m) and a characteristic hillslope breadth $B = 13$ km using the relationship $B = A/(2L)$.

4.3 Statistical uncertainty

Unless stated otherwise, all statistical uncertainties reported in this paper correspond to 95% confidence intervals around the mean. In addition, we include second-order interaction terms because τ, ϕ, and b are not independent. As described later, the error distributions on τ, ϕ, and b satisfy the normality assumption required by the following error propagation method (Taylor & Kuyatt, 1994).

The primary quantitative prediction made in this paper is the average rate of change of the active groundwater layer, $\mathrm{d}\bar{\eta}/\mathrm{d}t$, estimated via (23). To estimate the statistical uncertainty of $\mathrm{d}\bar{\eta}/\mathrm{d}t$ we combined the individual uncertainty estimates of each term in (23):

$$\widehat{\varepsilon}_{\mathrm{d}\bar{\eta}/\mathrm{d}t} = \mathrm{d}\bar{\eta}/\mathrm{d}t \sqrt{\left(\frac{\widehat{\varepsilon}_{\lambda}}{\lambda}\right)^{\mathbf{2}} + \left(\frac{\widehat{\varepsilon}_{\mathrm{d}\bar{Q}/\mathrm{d}t}}{\mathrm{d}\bar{Q}/\mathrm{d}t}\right)^{\mathbf{2}}}, \tag{30}$$

where:

$$\widehat{\varepsilon}_{\lambda} = \sqrt{\mathbf{J}\,\mathbf{V}\,\mathbf{J}^{\mathrm{T}}} \tag{31}$$

is the uncertainty of the sensitivity coefficient $\lambda = \tau/\phi[1/(N+1)]$, $\mathbf{J}$ is the Jacobian of λ, $\mathbf{V}$ is the covariance matrix of the sample populations $\{\tau, \phi, N\}$, and $\widehat{\varepsilon}_{\mathrm{d}\bar{Q}/\mathrm{d}t}$ is the uncertainty of the trend slope $\mathrm{d}\bar{Q}/\mathrm{d}t$ estimated via ordinary least-squares linear regression. Recall $N \sim 1/(2b)$ in (23) therefore $\widehat{\varepsilon}_N = 2\widehat{\varepsilon}_b$.

5 Application of theory to Kuparuk River Basin streamflow and active layer thickness data

5.1 Surface-based observational data

In this section, the theory proposed in Section 3 and Section 4 is applied to 38 years of daily streamflow data for the Kuparuk River on the North Slope of Arctic Alaska (70°16'54"N, 148°57'35"W) (Figure 2). The Kuparuk River drains an ~8400 km^2 catchment area that extends from the foothills of the Brooks Range northward to the Arctic Ocean along the Central Beaufort Coastal Plain. Catchment topography is characterized by low relief with mean elevation ~265 m a.s.l. and elevation range 10–1500 m a.s.l.. Catchment soils are comprised of alluvial marine and floodplain deposits and aeolian sand and loess, underlain by continuous permafrost >250 m thick. The Kuparuk basin-mean active layer thickness is thought to be less than one meter on average (McNamara et al., 1998; O'Connor et al., 2019).

Water levels were recorded at United States Geological Survey (USGS) gage 15896000 and converted to discharge by USGS personnel following USGS protocols (Rantz, 1982). Daily flows are reported to nominal 1 $ft^3\ s^{-1}$ precision. Stage and discharge accuracy are affected by fluvial incision and landscape degradation, by river ice and aufeis during winter (Huryn et al., 2021), and by ice jams and flooding during ice breakup. Annual USGS water-year summaries indicate automated ratings are replaced by estimated values due to aforementioned factors, and the actual precision of reported discharge varies from ~0.1 $ft^3\ s^{-1}$ for automated ratings to ~1000 $ft^3\ s^{-1}$ for estimated values.

Stage and discharge precision together define a minimum observable $-\mathrm{d}Q/\mathrm{d}t$ which may impart bias on estimated recession parameters (Rupp & Selker, 2006a). The effect of measurement precision for Kuparuk River flows is evident in estimated flow values below ~100 $ft^3\ s^{-1}$ (~2.5e^5 $m^3\ d^{-1}$), which typically occur during Oct–Nov prior to flow cessation from ~Dec–May (Figure 3a). The rapid flow increase following river ice breakup in late Spring partially masks the discretization of low-precision estimated values. As mentioned in Section 4.2, measurement discretization was remediated by use of an exponential time step to compute $\mathrm{d}Q/\mathrm{d}t$ (Roques et al., 2017). Note all flow data is converted to $m^3\ d^{-1}$ prior to fitting (3).

Active layer thickness is measured at nine locations within the Kuparuk River basin (Figure 2) (Nyland et al., 2021). The measurements used here were made by inserting small-diameter metal probes to point of refusal at regular intervals along grids or transects of

side-length ~100–1000 m. Mechanical probing is supplemented by thermistors measuring soil temperature at four sites. Data are reported as end-of-season averages believed to represent the annual maximum thaw depth (i.e., ALT). A continuous annual record from 1990–2020 is available for the Toolik Long Term Ecological Reserve site, from 1992–2020 for the Imnavait Creek site, and from 1995–2020 for other sites; all site data were averaged to create one continuous record for the Kuparuk River basin. The CALM program and the International Permafrost Association implemented standardized measurement protocols around 1995.

Precipitation is measured at a network of meteorological stations within and proximate to the catchment (Kane et al., 2021). Although gauge undercatch affects Arctic precipitation measurements, our goal is to determine if rainfall occurred rather than how much occurred, and undercatch is small (~10%) during the late summer recession period when wind speeds are lower (Yang et al., 2005). Daily precipitation measurements from 1983–2020 used in this study were measured at the National Oceanic and Atmospheric Administration Cooperative Observer Program station 505136 (Kuparuk station).

5.2 Topographic data

Catchment topography was provided by USGS digital terrain models for the state of Alaska derived from interferometric synthetic aperture radar (IFSAR) (Earth Resources Observation And Science (EROS) Center, 2018). These data were provided as tiles with elevations posted at 5 m horizontal resolution and clipped to the catchment outline using the Geospatial Data Abstraction software Library (Figure 2) (GDAL/OGR contributors, 2022).

5.3 Climate reanalysis and satellite observations

Climate reanalysis and satellite gravimetry data were used to close the annual water balance, which provides a method to infer permafrost thaw rate (Brutsaert & Hiyama, 2012). Climate reanalysis was provided by Modern-Era Retrospective Analysis for Research and Applications, version 2 (MERRA2) (Gelaro et al., 2017). Monthly terrestrial water storage anomalies were provided by University of Texas at Austin Center for Space Research CSR RL06 Gravity Recovery and Climate Experiment (GRACE) and GRACE Follow-On (GRACE-FO) mascon solutions (http://www2.csr.utexas.edu/grace) (Save et al., 2016). GRACE data is available on a monthly timestep for the period 2002–2020. Twenty-two missing values in the

GRACE timeseries and thirteen GRACE-FO values were gap-filled following Yi and Sneeuw, (2021).

The annual liquid water balance is defined as:

$$\frac{\mathrm{d}S_\ell}{\mathrm{d}t} = P - E - R + T \tag{32}$$

where P, E, and R (L/T) are annual sums of precipitation, evaporation, and runoff fluxes, and T (L/T) is a source term representing the catchment-mean permafrost thaw rate:

$$T = -\left(\frac{\rho_{\mathrm{ice}}}{\rho_{\mathrm{w}}}\right)\frac{\mathrm{d}\theta_{\mathrm{ice}}}{\mathrm{d}t} \tag{33}$$

where ρ_{ice} [M/L^3] is ice density, ρ_{w} [M/L^3] is liquid water density, and θ_{ice} [L^3/L^3] is volumetric soil ice content (the ratio of ice by volume to soil by volume).

GRACE water storage anomalies do not measure $\mathrm{d}S_\ell/\mathrm{d}t$ (32) but rather $(P - E - R)$ (and any other gain or loss of above- or below-ground mass). In contrast, $\phi\mathrm{d}\bar{\eta}/\mathrm{d}t$ as predicted via (20) is, in principle, comparable to (32), which shows that $\mathrm{d}\bar{\eta}/\mathrm{d}t$ is only attributable to T if $(P - E - R) = 0$. Therefore, we can attempt to detect T by rearranging (32):

$$T = \frac{\mathrm{d}S_B}{\mathrm{d}t} - (P - E - R) \tag{34}$$

where $S_B = S - S_{\mathrm{ref}}$ is storage anomaly at time t detected with baseflow recession analysis as in (6). Alternatively:

$$T = \frac{\mathrm{d}S_B}{\mathrm{d}t} - \frac{\mathrm{d}S_G}{\mathrm{d}t} \tag{35}$$

where S_G is GRACE terrestrial water storage anomaly at time t.

In practice, $\mathrm{d}S_B/\mathrm{d}t$ was estimated by bringing ϕ to the left-hand side of (20) and regressing the right-hand side $\tau_{\mathrm{r}}/(N+1)\bar{Q}$ against time in years. Similarly, $\mathrm{d}S_G/\mathrm{d}t$ was estimated via regression of annual August–October minimum S_G anomalies (which is used as a proxy for catchment storage during the streamflow recession period) against time in years. In this way, both (34) and (35) yield estimates of the average thaw rate T over the time interval represented by $\mathrm{d}t$, which ranges from 18–37 years for S_B, and 18 years for S_G (Section 5.4.3). For 16 out of 19 years, the annual minimum S_G occurred in August–October, which coincides

with the streamflow recession period. In 2018, S_G reached a minimum in January and then a second local minimum in September. Similarly, in 2010 and 2019 S_G reached local minima in November and July, respectively, with magnitudes nearly identical to adjacent October and August values. To obtain a comparable estimate of $\mathrm{d}S/\mathrm{d}t$ from MERRA2 reanalysis, we compute $(P-E-R)$ on a water year basis such that $(P-E-R)_i$ represents $\mathrm{d}S/\mathrm{d}t$ over a period from October 1 of year $i-1$ to September 30 of year i.

5.4 Comparison of theory with data in the Kuparuk River basin

5.4.1 Drainable porosity

Estimates of ϕ obtained from the point-cloud method and the event-based method indicate a characteristic value of $\langle\phi\rangle \cong 0.05$, with moderate sensitivity to (26)–(28) (Figure 4). Substitution of the respective point-cloud intercepts a_1 and a_2 into (26)–(28) yielded $\phi = 0.04-0.09$, depending on late-time $b=1$, $b=3/2$, and $\hat{b}=1.32$ (Section 4.2). The event-based method yielded a narrower range of values between 0.03–0.05 with relative uncertainties of ~30–50% (Figure 4). Note that $\hat{b}=1.32$ implies an inverted $k(z)$ profile in the context of (5) with $n \cong -1/2$, which is inconsistent with field observations of $k(z)$ in the upper Kuparuk River basin (Figure 5) (O'Connor et al., 2019). Estimates based on (28) may therefore be unreliable. To mitigate this, we construct an estimate based on (26) and (27). The justification is that $b=1$ and $b=3/2$ bracket $\hat{b}=1.32$ without assuming an inverted $k(z)$ profile. Combining all event-based ϕ values from (26) and (27) into one sample, we obtain a Beta distribution fit $\langle\phi\rangle \cong 0.046 \pm 0.009$ (Figure 4), which is used in all results hereafter.

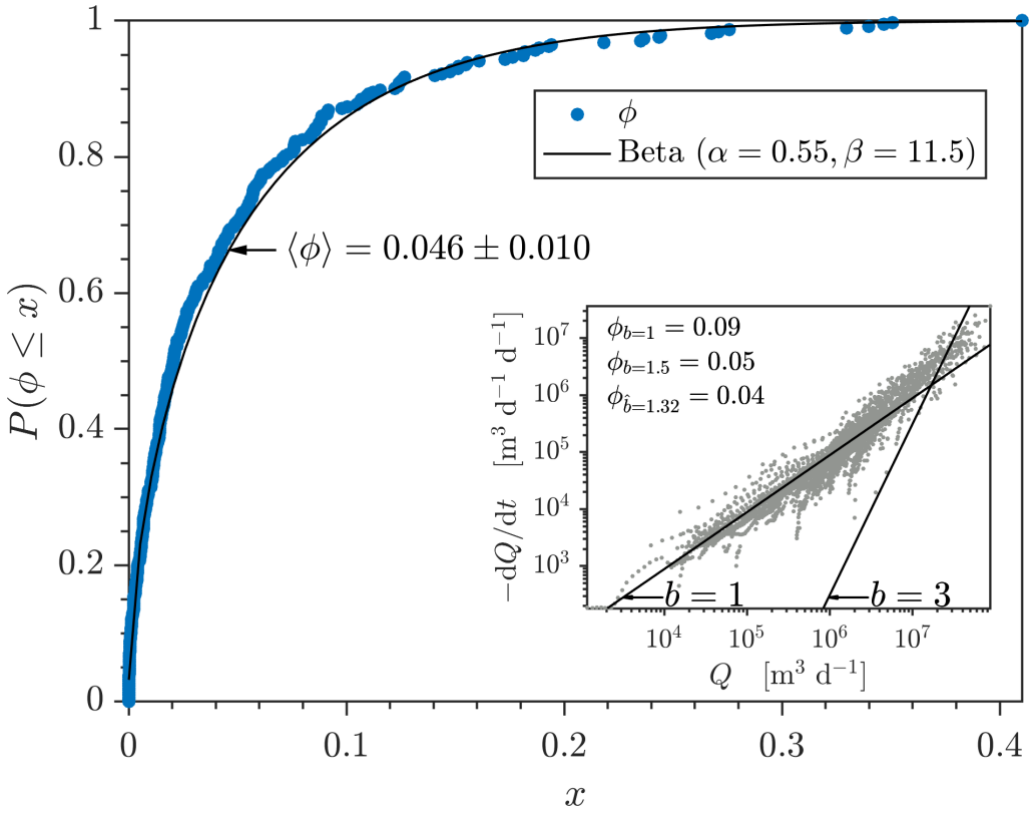

Figure 4: (main panel) Cumulative probability distribution of drainable porosity ϕ estimated from individual recession events with Equation 26 and Equation 27 (blue circles) and the best-fit Beta distribution (solid black line). The expected value of ϕ is indicated by arrow. (inset) Example of the point-cloud method to estimate ϕ with Equations 26–28, using values of early-time intercept a_1 for a line of slope $b = 3$, and late-time intercept a_2 for lines of slope $b = 1$, $b = 3/2$, and $\hat{b} = 1.32$ (inset shows $b = 3$ and $b = 1$ for demonstration; ϕ estimated with each of Equations 26–28 are printed upper left).

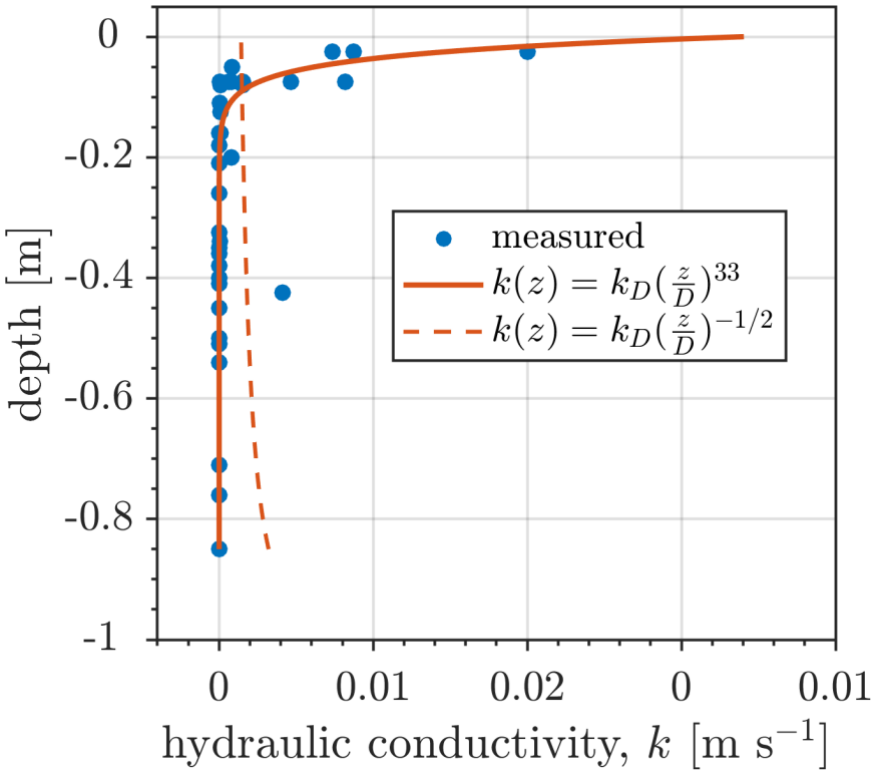

Figure 5: Saturated hydraulic conductivity (solid circles) measured at Imnavait Creek Research Station in the Kuparuk River basin (O'Connor et al., 2019) and the best-fit nonlinear least-squares power-function (solid line). The best-fit exponent $n \cong 33$ corresponds to $b = 1.97$ for both flat- and sloped-aquifer solutions ($b \to 2$ for $n \gg 10$ for both solutions). The best-fit value obtained from recession analysis $\hat{b} = 1.32$ ($n \cong -1/2$) predicts an inverted saturated hydraulic conductivity profile (dashed line), which is inconsistent with the measurements.

5.4.2 Drainage timescale and expected value of baseflow

The Pareto distribution fit to τ yielded an estimate of $\hat{\tau}_0 = 13 \pm 1$ days and $\langle\tau\rangle = 25 \pm 4$ days (Figure 6). The estimated exponent $\hat{\alpha} = 3.11 \pm 0.44$ corresponds to $\hat{b} = 1.32 \pm 0.04$. A total of 3,010 τ values were obtained from 186 recession events, of which 1,203 values exceeded τ_0 (Figure 7, red circles). Note that an individual τ value may exceed τ_0 but occur within an event of duration $t < \tau_0$ (96 events exceeded $\hat{\tau}_0$ in duration). The $\hat{\alpha}$, $\hat{\tau}_0$ and $\langle\tau\rangle$ parameter ensembles constructed by bootstrap resampling (Section 4.1) from the 1,203 $\tau \geq \hat{\tau}_0$ values were symmetric about the mean to within the ~one-day and ~four-day precision.

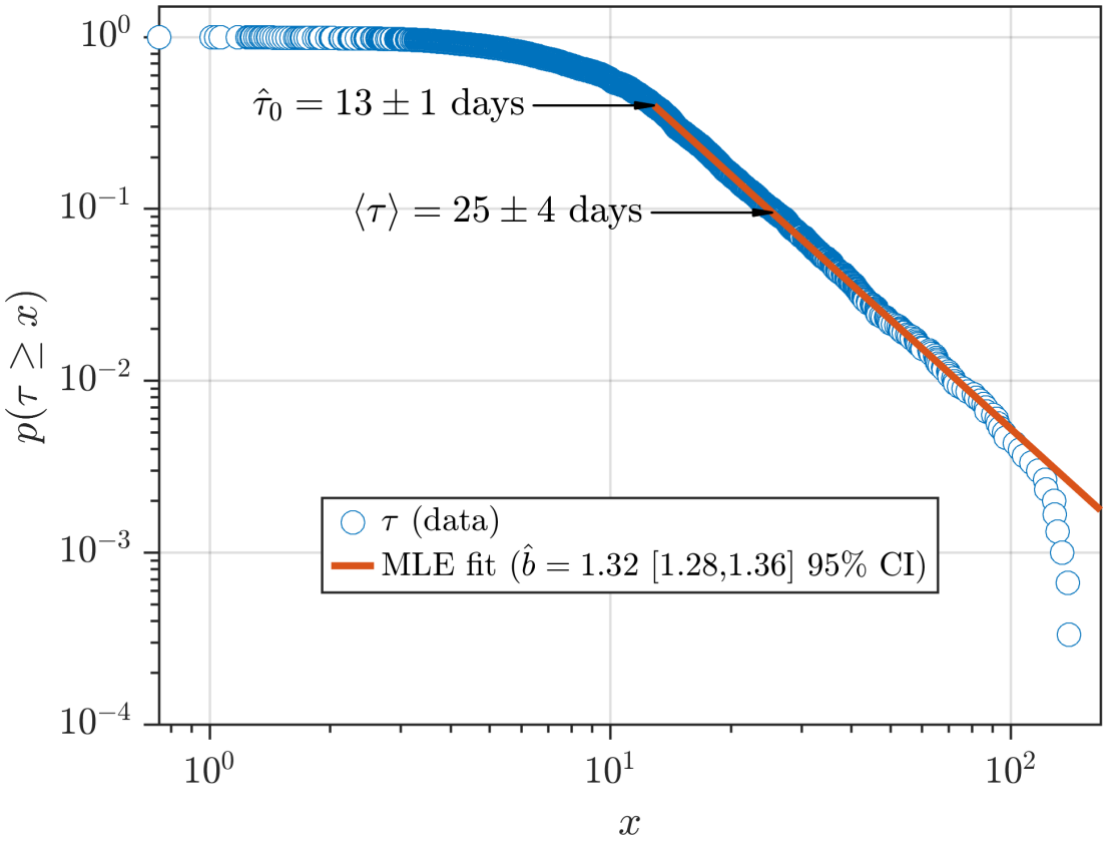

Figure 6: Complementary cumulative (exceedance) probability for drainage timescale τ (blue circles) and the maximum likelihood estimate (MLE) best-fit Pareto distribution (solid red line). The theoretical distribution (Equation 12) is fit to $\tau > \tau_0$, where $\tau_0 = 13$ days is the threshold timescale beyond which baseflow scales as a power-law. The expected value $\langle\tau\rangle = 25$ days is the average drainage timescale given the best-fit parameter $\hat{b} = 1.32$. Confidence intervals are two standard deviations of a bootstrapped ensemble (N=1000). The falloff at $\tau > 100$ days is indicative of finite system size effects which occur when the underlying population is under-sampled at extreme values but may also indicate a process transition to linear scaling as $Q \to 0$.

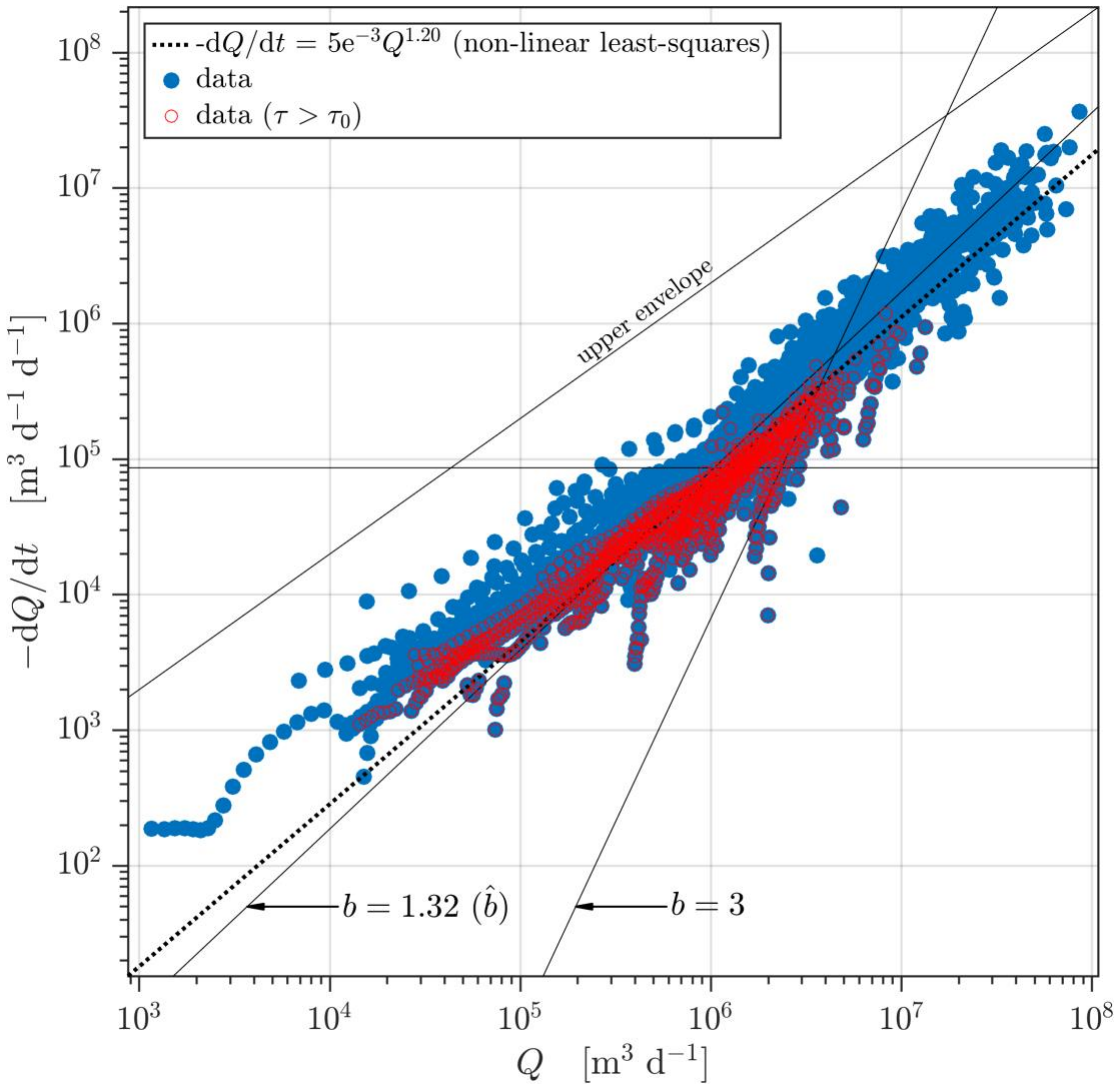

Figure 7: Point-cloud diagram showing 3,010 values of Q and $-\mathrm{d}Q/\mathrm{d}t$ from 186 detected recession events and a line of slope $\hat{b} = 1.32$ obtained from $b = 1 + 1/\alpha$ (Equation 25) compared with a line of slope $b = 1.20$ (dotted) obtained from nonlinear least-squares fit to the point cloud. Values of $Q \in (\tau > \tau_0)$ are highlighted with red circles. Reference lines are described in Figure 3.

The Pareto fit to τ does not provide $\langle Q \rangle$ nor $\hat{Q}_0$, although they could be obtained from a similar modeling procedure. Instead, a value of $\hat{Q}_0 = 10$ m^3 s^{-1} (Figure 3a, dotted line) consistent with $\hat{\tau}_0 = 13$ days and $\hat{b} = 1.32$ was obtained from (9), similar to the method used to obtain $\hat{a}$ (Section 4.1). In this context, $\hat{Q}_0$ is an estimate of the threshold value of Q below which baseflow scales as a power-law, and the theory outlined herein can be expected to make reasonable predictions. The value 10 m^3 s^{-1} maps to the 36th percentile of the daily flow and is similar to the mean October flow ~13 m^3 s^{-1}. From (13), it predicts a value for expected baseflow $\langle Q \rangle = 3.6$ m^3

535 s^{-1}, which maps to the 26th percentile of daily flow (Figure 3a, dashed line). The mean daily flow
536 is ~80 m^3 s^{-1}.

537 On this basis, the long-term baseflow trend $\mathrm{d}\bar{Q}/\mathrm{d}t$ was estimated by quantile regression
538 on the 26th percentile of the annual timeseries of mean daily flow (Figure 8). That is, $\mathrm{d}\bar{Q}/\mathrm{d}t$ is
539 the trend in the flow percentile nearest $\langle Q \rangle$, the expected value of baseflow. Although we would
540 prefer to estimate $\mathrm{d}\bar{Q}/\mathrm{d}t$ from an annual timeseries of $\langle Q \rangle$, there is insufficient data to fit (12) on
541 an annual basis. The baseflow timeseries is hereafter $\bar{Q}$, but it should be recognized that $\bar{Q}$ is the
542 26th percentile of the annual timeseries of mean daily flow.
543

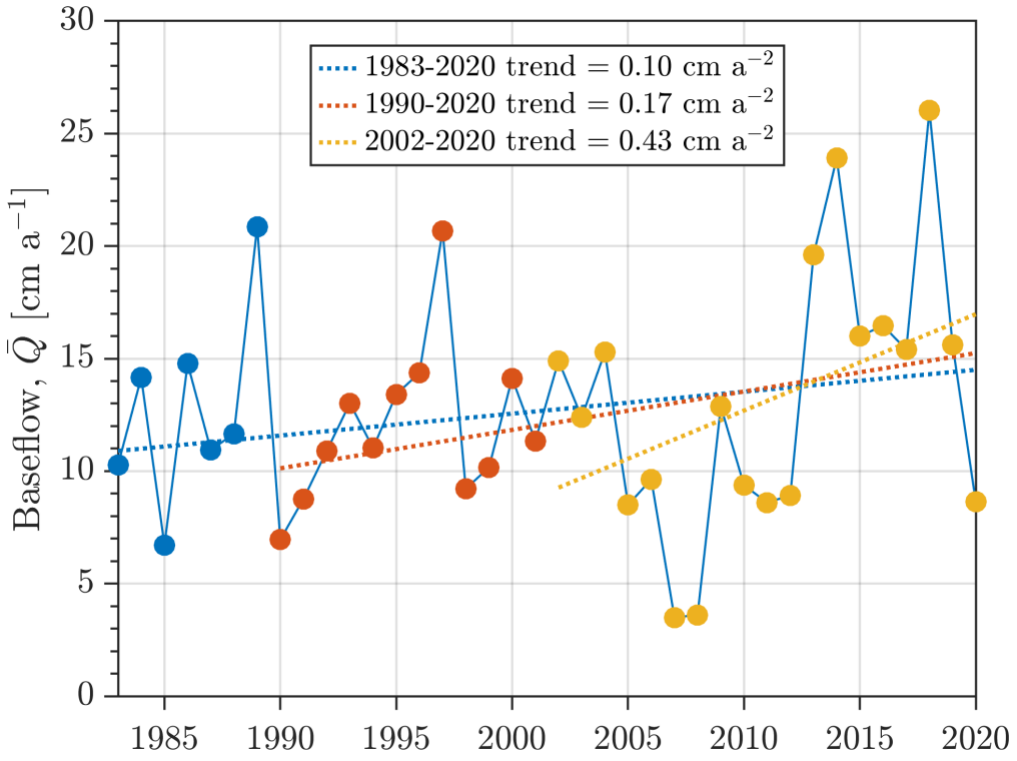

Figure 8: Linear trend in the 26th percentile of daily flow on an annual basis for three periods examined in this study. The expected value of baseflow $\langle Q \rangle = 3.6$ m^3 s^{-1} (13 cm a^{-1}) corresponds to the 26th percentile of daily flow and is used in this study as a proxy for annual average baseflow $\bar{Q}$. The 26th percentile of daily flow is the value of the flow duration curve having an exceedance probability of $1 - 0.26 = 0.74$.

5.4.3 Active groundwater layer thickness from recession analysis and observations

Three periods are examined, as dictated by data availability: 1983–2020 covers the period of overlapping precipitation and discharge measurements; 1990–2020 adds ALT measurements; 2002–2020 adds GRACE data. From 1983–2020, observed mean annual flow increased 0.24 ± 0.15 cm a^{-2} and $\bar{Q}$ increased 0.10 ± 0.10 cm a^{-2} (Figure 8). From 1990–2020, these rates increased to 0.31 ± 0.21 cm a^{-2} and 0.17 ± 0.21 cm a^{-2}, respectively. During this period, measured ALT increased 0.31 ± 0.22 cm a^{-1}, and $\bar{\eta}$ estimated with (23) increased 0.20 ± 0.24 cm a^{-1} (Figure 9). Converted to liquid water thickness using $\langle \phi \rangle$, the trend in measured ALT converts to an active layer infilling rate of 0.014 ± 0.010 cm a^{-1}, ~55% larger than $\mathrm{d}S_B/\mathrm{d}t = 0.009 \pm 0.011$ cm a^{-1} estimated with (23). This suggests the saturated groundwater layer increased at a slower rate than the actual active layer, and a surplus of thaw water in excess of $\mathrm{d}\bar{\eta}/\mathrm{d}t$ contributed to the observed increase in $\bar{Q}$ during this period. Water balance trends are reported in Section 5.4.4.

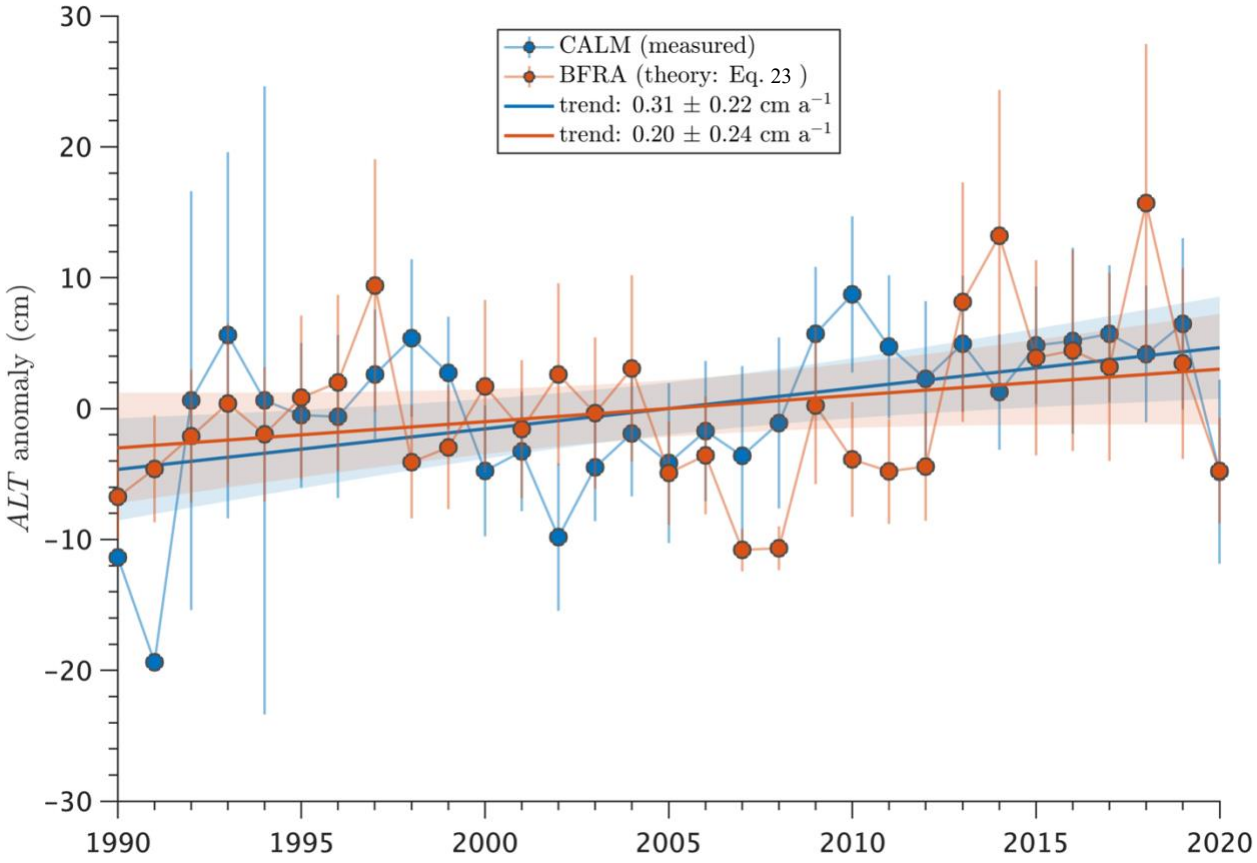

Figure 9: Linear trend in active layer thickness from field measurements in the Kuparuk River basin provided by the Circumpolar Active Layer Monitoring (CALM) program (Nyland et al., 2021) (blue error bars and blue trend lines) compared with linear trend in active groundwater layer thickness predicted with baseflow recession analysis (BFRA) (Equation 23) (red error bars and red trend lines). Error bars for CALM data are two standard errors scaled by a critical t-value (95% confidence intervals); sample size varies from one site (Toolik LTER) (1990 and 1991) to nine (1995-2020) as additional monitoring sites were established. Error bars for BFRA predictions are 95% confidence intervals computed with Equation (31) (Section 4.3). Shaded error bounds are 95% confidence intervals for the linear trend lines. Error margins printed in the legend are 95% confidence intervals for the regression slope coefficients.

During 2002–2020, these trends approximately doubled (Figure 10). Measured ALT increased 0.53 ± 0.37 cm a^{-1}, $\bar{\eta}$ estimated with (23) increased 0.50 ± 0.59 cm a^{-1}, and GRACE terrestrial water storage converted to soil layer thickness via $\eta_G = S_G/\phi$ increased 0.80 ± 3.4 cm a^{-1}. In terms of liquid water thickness, the observed ALT trend converts to an infilling rate 0.024 ± 0.017 cm a^{-1}, ~5% higher than $\mathrm{d}S_B/\mathrm{d}t = 0.023 \pm 0.027$ cm a^{-1} estimated with (23) and ~34% lower than $\mathrm{d}S_G/\mathrm{d}t = 0.036 \pm 0.15$ cm a^{-1}. The observed mean annual flow increased 0.57 ± 0.50 cm a^{-2} and $\bar{Q}$ increased 0.43 ± 0.50 cm a^{-2} (Figure 8).

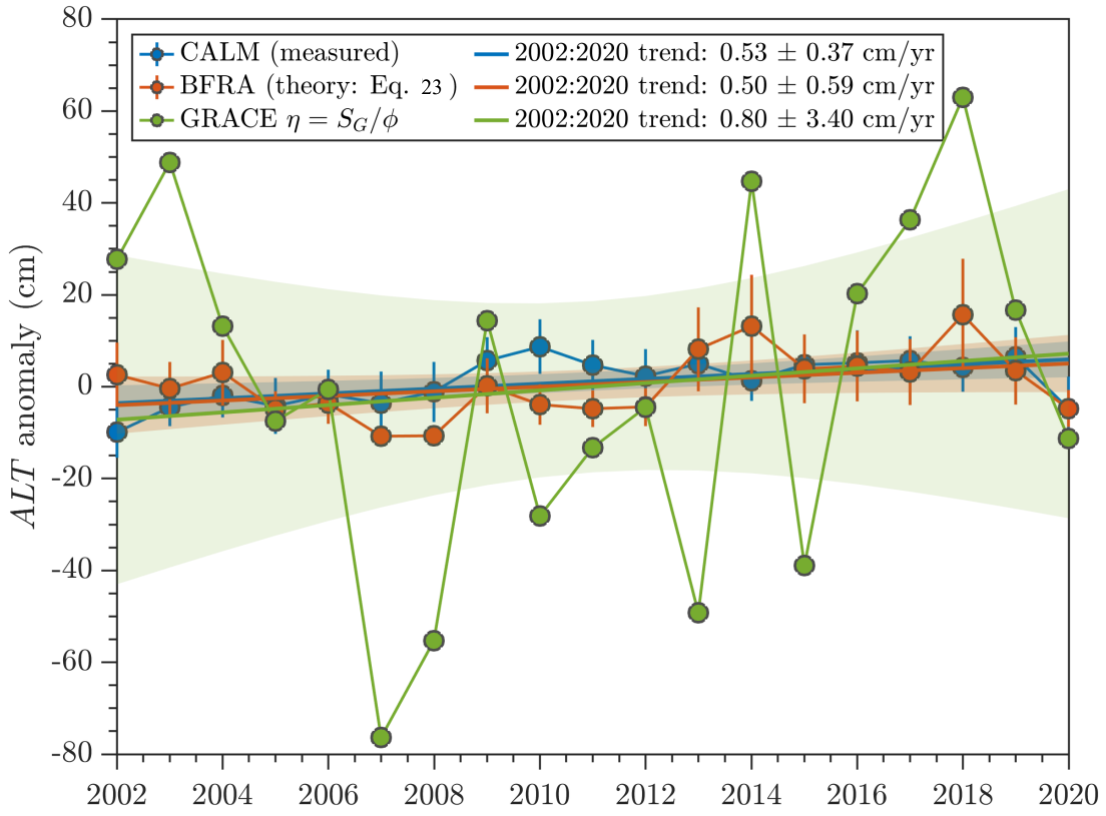

583

584 **Figure 10**: Linear trend in GRACE terrestrial water storage anomalies (green circles and green trend line)
585 and (as in Figure 9) active layer thickness from field measurements (blue error bars and blue trend lines)
586 compared with baseflow recession analysis predictions (red error bars and red trend lines). GRACE
587 storage anomalies are converted to equivalent groundwater layer thickness using $\phi = 0.05$ inferred from
588 baseflow recession. Error bars and error bounds are described in Figure 9.

589 **5.4.4 Interpreting groundwater storage trends in terms of catchment water balance**

590 As mentioned in Section 5.3, the trend in $\bar{\eta}$ can only be attributed to permafrost thaw if
591 $P - E - R = 0$. During 1990–2020, MERRA2 reanalysis indicates catchment-mean P increased
592 0.22 ± 0.29 cm a^{-2}, balanced by an increase in E and R of 0.01 ± 0.07 cm a^{-2} and 0.21 ± 0.23
593 cm a^{-2}, respectively, leaving a negligible residual trend in $(P - E - R)$. In this context, the
594 acceleration of P was balanced almost entirely by R and a small acceleration of E. However, the
595 annual average water-year $(P - E - R)$ was ~1.04 cm a^{-1}, well in excess of $\mathrm{d}S_B/\mathrm{d}t$. Strictly
596 speaking, this suggests $\mathrm{d}S_B/\mathrm{d}t$ and $\mathrm{d}\bar{Q}/\mathrm{d}t$ cannot be attributed to permafrost thaw during this
597 period, because the excess $(P - E - R)$ is sufficient to explain all of the increase in S_B and $\bar{Q}$,
598 and then some. This is discussed further in Section 6.

599 Turning to the GRACE period (2002–2020), MERRA2 reanalysis indicates
600 catchment-mean P increased 0.59 ± 0.68 cm a^{-2}, balanced by an increase in E and R of $0.05 \pm$

601 0.15 cm a^{-2} and 0.52 ± 0.52 cm a^{-2}, respectively, leaving a residual acceleration in $(P - E - R)$
602 of 0.03 ± 0.47 cm a^{-2}. The annual average water-year $(P - E - R)$ was ~0.98 cm a^{-1}, again, well
603 in excess of $\mathrm{d}S_B/\mathrm{d}t$. However, these values are also well in excess of $\mathrm{d}S_G/\mathrm{d}t = 0.036$ cm a^{-1}, as
604 reported in Section 5.4.3. This appears robust: if $\mathrm{d}S_G/\mathrm{d}t$ is approximated by annual differences
605 of annual-average S_G on a water-year basis (rather than linear regression), $\mathrm{d}S_G/\mathrm{d}t = 0.06$ cm a^{-1}.

606 We tested various alternative definitions of $\mathrm{d}S_G/\mathrm{d}t$ including annual calendar-year
607 differences ($\mathrm{d}S_G/\mathrm{d}t = 0.024$ cm a^{-1}), annual differences of the annual maximum S_G ($\mathrm{d}S_G/\mathrm{d}t =$
608 0.25 cm a^{-1}), and annual differences of the average August–October S_G ($\mathrm{d}S_G/\mathrm{d}t = -0.08$ cm
609 a^{-1}). The largest values of $\mathrm{d}S_G/\mathrm{d}t$ obtained were for Northern Hemisphere winter months, but
610 none approached the magnitude of MERRA2 water-year $(P - E - R)$. Subtraction of MERRA2
611 snow mass anomalies from S_G yielded different estimates of $\mathrm{d}S_G/\mathrm{d}t$ but did not change the
612 conclusion that MERRA2 $(P - E - R)$ substantially exceeded both $\mathrm{d}S_G/\mathrm{d}t$ and $\mathrm{d}S_B/\mathrm{d}t$.
613 Consequently, (34) is unlikely to provide meaningful estimates of T.

614 ## 6 Discussion

615 ### 6.1 Active layer thickness and saturated soil layer thickness change

616 We find that the saturated soil layer thickened between 1983–2020 in the Kuparuk River
617 basin, in agreement with field measurements of ALT in the region (Nyland et al., 2021). This
618 finding was enabled by new theoretical relationships between basin outflow during streamflow
619 recession and the rate of change of the active groundwater layer (Section 3), using the principles
620 of hydraulic groundwater theory (Brutsaert, 2005). Specifically, we extended an earlier linear
621 reservoir theory (Brutsaert & Hiyama, 2012) to the nonlinear case. This provides a physical
622 interpretation of the relationship between ALT trends and baseflow trends for river basins with
623 nonlinear empirical storage-discharge relationships. It is important to acknowledge that this
624 approach dramatically simplifies real-world permafrost hydrology, yet appears to provide
625 reasonable predictions for the studied area. Although a thorough comparison with more
626 observations is needed to build confidence, the framework developed here may open the door to
627 retrospective estimation of ALT trends in data sparse Arctic catchments with short, sporadic, or
628 even nonexistent ground-based active layer measurements.

A first application of the theory to 38 years of Kuparuk River streamflow indicates the active groundwater layer thickened ~4.4 cm during this time. The rate of increase nearly doubled between 1990–2020 for a total increase of ~6.2 cm. Direct measurements of the actual active layer thickness made during this period indicate an increase of ~9.6 cm. Although the plot-scale, site-averaged observed rate of change is +55% higher than the basin-scale theoretical prediction, both are consistent with observations of thickening active layer and a growing importance of subsurface hydrologic processes in the region (Arp et al., 2020; Luo et al., 2016; Rawlins et al., 2019; Rowland et al., 2011).

A similar picture emerged for the period 2002–2020, during which time observations of terrestrial water storage (TWS) from the GRACE and GRACE-FO satellites are available to aid interpretation. First, relative to 1990–2020, the inferred rate of increase of the active groundwater layer more than doubled again, in close agreement (+5%) with direct field measurements of the actual active layer thickness. In terms of liquid-water-equivalent storage, TWS anomalies increased ~50% more each year on average than predicted increases in active groundwater layer storage, albeit with uncertainties that exceed all reported trends. Under an idealized assumption that melted ice remains stored as liquid water (or is discharged and later replaced by precipitation) GRACE would detect no mass change. TWS trends are therefore not directly comparable to active groundwater layer storage trends predicted from baseflow recession, but rather indicate whether a surplus or deficit of water was available each year to support filling or draining of active layer.

Climate reanalysis and streamflow observations indicate that both precipitation and runoff are increasing in the Kuparuk River basin, at rates far exceeding inferred increases in water storage in thicker active layer over all periods examined. Focusing on 2002–2020, MERRA2 climate reanalysis indicates the annual average ($P - E - R$) was positive (~1 cm a^{-1}), and about twice as large when computed using observed discharge Q rather than climate reanalysis R (this holds over all periods examined). Moreover, the trend in MERRA2 P outpaced the trend in $E + R$ leaving a residual acceleration in ($P - E - R$). The acceleration suggests a smaller (~0.5 cm a^{-1}) average annual increase but remains an order of magnitude larger than predicted increases in active layer storage and TWS anomalies. Taken together, this suggests a surplus of precipitation was available to drive observed increases in discharge and storage in

thicker active layer, which precludes attribution of either discharge or ALT trends to thawing permafrost.

Although climate reanalysis and satellite gravimetry are too coarse to resolve <0.1 cm a^{-1} trends in active layer storage, the decisively positive ($P - E - R$) supports an interpretation that the active layer was effectively saturated throughout the studied period. One consequence is that (34) and (35) cannot be expected to provide meaningful estimates of catchment-effective thaw rate, which was already unlikely given their simplification of active layer and the scale mismatch between reanalysis, GRACE, and ~8400 km^2 Kuparuk River basin. However, it also suggests the active groundwater layer thickness likely increased in proportion to the actual active layer thickness, and that predicted trends are candidate proxies for actual trends. If ($P - E - R$) were decisively negative, predicted trends in active groundwater layer thickness would likely under-predict actual active layer trends owing to loss of storage to $E + R$ (Brutsaert & Hiyama, 2012). Climate reanalysis and satellite gravimetry may therefore prove useful for interpreting recession analysis predictions at broad scales and in regions without ground-based observations.

6.2 Limitations of the method and suggestions for future research

Section 3 presents a dramatic simplification of active layer hydrology, and we discuss a few salient criticisms. First, (1) acquires physical meaning from solutions to (4) that assume instantaneous drawdown of an initially saturated Boussinesq aquifer discharging to a fully- or partially-penetrating channel (Brutsaert & Nieber, 1977; van de Giesen et al., 2005; Rupp & Selker, 2005). This implies negligible influence of precipitation, evaporation, channel routing, overland flow, unsaturated flow, deep groundwater flow, and anything else that affects recession. Rather than assume negligible evaporation, future work could incorporate frameworks that include evaporation in (3) (Szilagyi et al., 2007; Zecharias & Brutsaert, 1988b) into the derivation that leads to (20).

Transient recharge, unsaturated flow, and aquifer compressibility, the latter of which is particularly relevant to thawing permafrost (Liljedahl et al., 2016), are thought to mainly affect early-time recession (Liang et al., 2017). This suggests possible bias when estimating ϕ from early-time solutions using (26)–(28), which is a critical uncertainty because ϕ is a small number in the denominator of (20). The actual aquifer-contributing area may also be smaller than the basin area. If so, the value of A in (26)–(28) is biased high and ϕ is biased low. This may explain

why ϕ estimates obtained from the method of (26)–(28) appear systematically low compared with field-scale estimates (c.f. Equation 15 of Brutsaert & Nieber, 1977). Deep groundwater flow paths, which are indicated by isolated aufeis in the lower reaches of the Kuparuk (Huryn et al., 2021), are expected to have a similar effect (Liang et al., 2017).

Precipitation was mitigated by censoring flows within a six-day window of recorded rainfall if a streamflow response was detected, whereas most prior works detected rainfall from the streamflow response alone (Brutsaert & Hiyama, 2012; Cheng et al., 2016; Dralle et al., 2017; Evans et al., 2020; many others). Using rainfall measurements to censor flows resulted in fewer detected recession events, as expected. However, it unexpectedly eliminated the smallest detected baseflow values because rainfall is common during Oct–Nov when the lowest baseflows occur in the studied area. This reduced $\langle\tau\rangle$ because τ is inversely proportional to Q for $b > 1$, and may have contributed to the falloff at $\tau > \sim 100$ days (Figure 6). This is a specific example of a general result that $\langle\tau\rangle$ depends on the sample space of Q, and indicates a possible low bias in $\langle\tau\rangle$ from under-sampling the lowest flows. The inferred magnitude $\langle\tau\rangle \cong 25$ days is about two-thirds the canonical value 45 days obtained from linear recession analysis, whereas $\langle t\rangle \cong 36$ days is within the ± 15 day characteristic uncertainty (Brutsaert, 2008; Brutsaert & Sugita, 2008; Cooper et al., 2018). A detailed study of τ sensitivity to methodology is needed and would likely benefit from numerical simulation in addition to empirical estimation (c.f., Rupp et al., 2009).

6.3 Implications for recession analysis and hydrologic signatures

In Section 3 we showed that the nonlinear drainage timescale τ follows an unbounded Pareto distribution and a method to fit the distribution that provides an unbiased estimate of b in the event-scale recession equation $-\mathrm{d}Q/\mathrm{d}t = aQ^b$. This provides an alternative to ordinary least-squares fitting to a bi-logarithmic plot of Q versus $-\mathrm{d}Q/\mathrm{d}t$. In addition to retaining large-sample information, a key benefit of this method is the absence of parameter a in the fitting procedure. When individual recession events are plotted on a traditional point cloud diagram, events with similar slope b but different intercept a produce a characteristic offset (Biswal & Kumar, 2014; Jachens et al., 2020; Zecharias & Brutsaert, 1988a). A linear fit to the point cloud systematically underestimates b, in a manner analogous to the bias induced by least squares fitting to bivariate data with errors present in the independent variable (York et al., 2004). A remarkable by-product of the procedure developed here is shown in Figure 7, where the detected

sample of underlying power-law distributed recession flows (red circles) occupy exactly that portion of the point cloud where expert judgment would expect, far from the upper envelope, near the smallest values of $-\mathrm{d}Q/\mathrm{d}t$ for given Q (Brutsaert & Nieber, 1977; Rupp & Selker, 2006a).

This procedure also revealed that the drainage timescale τ is equal to the threshold τ_0 plus a timescale dictated by the degree of nonlinearity encoded in b:

$$\langle\tau\rangle = \tau_0 + (b-1)\langle t\rangle. \tag{36}$$

This way of writing (10) has important implications for the use of characteristic timescales as quantitative metrics of streamflow ('hydrologic signatures') (McMillan, 2020). It reveals that a threshold exists below which theoretical late-time power-law scaling of baseflow is not realized. Because $\langle\tau\rangle$ and τ_0 together determine $\langle t\rangle$ (the average duration of baseflow), they are directly linked to water availability. Thresholds dictating the onset of critical behavior are thoroughly understood generally (Aschwanden, 2015), and in porous media (Hunt & Ewing, 2009), but appear underexplored within the literature linking baseflow recession to hydrologic signatures (McMillan, 2020). At hillslope scales, τ_0 can be interpreted as a timescale representing the critical transition from "intermediate" ($2 < b < 3$) to "late-time" ($1 \leq b < 2$) recession (van de Giesen et al., 2005; Rupp & Selker, 2006b). At catchment scales, τ_0 represents a transition from disordered to ordered flow dictated by a combination of threshold-like processes that remain poorly understood (Troch et al., 2009).

7 Conclusions

We developed a theoretical framework to predict the long-term average rate of change of permafrost active layer thickness using principles of hydraulic groundwater theory and nonlinear baseflow recession analysis. Our method requires measurements of streamflow recession and catchment topography, and therefore has potential to complement or extend the spatial and temporal coverage of direct active layer measurements where few or none exist. Relative to earlier equations derived from linear reservoir theory, our nonlinear analysis (Section 3) predicts active layer may increase, decrease, or remain constant, depending on catchment topographic slope, saturated lateral hydraulic conductivity, and the degree of nonlinearity in the catchment storage-discharge relationship (or lack thereof). Critically, this implies that no unique functional relationship exists between active layer thickness change and streamflow change within the

749 context of baseflow recession analysis, and calls for further comparison with active layer
750 thickness measurements before the method is applied broadly.

751 A first application of our method to 38 years of daily streamflow observations in the
752 Kuparuk River on the North Slope of Arctic Alaska suggests the active layer thickened by ~4.4
753 cm between 1983–2020 and by ~6.2 cm between 1990–2020. Direct measurements of active
754 layer thickness during the latter period indicate the active layer thickened at a rate ~55% higher
755 than predicted. This suggests either the measurements overestimate the catchment-mean rate, or
756 the baseflow prediction is too low. The predicted rate of change more than doubled between
757 2002–2020, this time in closer agreement (+5%) with the observed rate. The inferred increase in
758 subsurface water storage was corroborated by satellite gravimetry and climate reanalysis, which
759 both indicate terrestrial water storage increased at rates that outpaced increases in subsurface
760 water storage as the active layer thickened in response to permafrost thaw.

761 Overall, these findings suggest that both increased precipitation and permafrost thaw are
762 playing increasingly important roles in sustaining baseflow in the Kuparuk River basin, and point
763 to a growing importance of subsurface hydrologic processes in the region. Nonlinear baseflow
764 recession analysis has potential to provide novel insight into these processes at the scale of river
765 basins, and we provide a consistent analytical framework to explore them.

Glossary

a, b	General discharge recession constants.
a_1, b_1	Early-time discharge recession constants.
a_2, b_2	Late-time discharge recession constants.
A	Horizontal aquifer area, equal to $2LB$.
ALT	Active layer thickness.
B	Aquifer breadth (distance along land surface).
c_1, c_2	Generic constant coefficients.
D	Aquifer thickness.
E	Evaporation per unit time.
h	Water table thickness.
h_0	Water table thickness at channel seepage face.
I	Recharge per unit time.
K	Aquifer drainage timescale for linear reservoir model.
k	Saturated lateral hydraulic conductivity.
k_D	Saturated lateral hydraulic conductivity at top of aquifer (entire aquifer if k is constant).
L	Channel or stream length.
n	Exponent of hydraulic conductivity power-function.
N	Exponent of discharge recession constant a power-function.
P	Precipitation per unit time.
q	Aquifer discharge per unit width of aquifer.
Q	Aquifer discharge, assumed equal to $2qL$; measured discharge assumed to be baseflow.
Q_0	Threshold aquifer discharge at onset of late-time recession.
$\bar{Q}$	Average aquifer discharge, assumed to equal average value of baseflow for timescales >1 year.
R	Runoff per unit time.
S	Aquifer storage.
$\bar{S}$	Average aquifer storage.
S_c	Critical aquifer storage at which discharge Q equals Q_{min}.
S_r	Reference aquifer storage (arbitrary datum).
T	Thaw per unit time.
t	Time.
x	Horizontal coordinate.
z	Vertical coordinate.
α	Exponent of Pareto distribution.
β	Exponent of storage-discharge function.
ε	Uncertainty interval half-width (error-margin).
ζ	Exponent of generalized Pareto distribution.
λ	Sensitivity coefficient, equal to $\tau/\phi[1/(N+1)]$.
η	Average water table thickness during aquifer drawdown.
$\bar{\eta}$	Average water table thickness.
ϕ	Drainable porosity.
θ	Aquifer slope above horizontal base.
σ	Scale parameter of generalized Pareto distribution.
τ	Aquifer drainage timescale for nonlinear reservoir model.
τ_0	Threshold aquifer drainage timescale at onset of late-time recession.
τ_r	Reference aquifer drainage timescale for nonlinear reservoir model.
μ	Threshold parameter of generalized Pareto distribution.
$\langle\ \rangle$	Expected value of probability distribution.
$\hat{}$	Parameter estimate.

Appendix A

A1 Particular solutions to the 1-D lateral groundwater flow equation

A1.1 Horizontal aquifers

Here we write particular forms of (20) and (22) based on late-time solutions to the 1-D lateral flow equation for horizontal (hereafter 'flat') aquifers (Boussinesq, 1903, 1904; Rupp & Selker, 2005). In doing so, we recover the earlier linear forms of (20) and (22) given in Brutsaert and Hiyama (2012). It is helpful to first recapitulate that the parameters a and b can be interpreted as solutions to the 1-D lateral flow equation for both flat and sloped aquifers:

$$\frac{\partial h}{\partial t} = \frac{k}{\phi}\frac{\partial}{\partial x}\left[h\left(\frac{\partial h}{\partial x}\cos\theta + \sin\theta\right)\right] + \frac{I}{\phi}, \qquad (A1)$$

where $h(x,t)$ is the phreatic water surface along dimension x, k is lateral saturated hydraulic conductivity, θ is bed slope, and I is recharge rate.

Detailed descriptions of $(A1)$ are widely available (e.g., Daly & Porporato, 2004); for our purposes, we note a particular form of $(A1)$ relevant to this analysis obtained by allowing k to vary as a power function of distance along the dimension z perpendicular to the impermeable base (Beven, 1982; Rupp & Selker, 2006b):

$$\frac{\partial h}{\partial t} = \frac{k_D}{\phi}\frac{D^{-n}}{(n+1)}\frac{\partial}{\partial x}\left[h^{n+1}\left(\frac{\partial h}{\partial x}\cos\theta + \sin\theta\right)\right] + \frac{I}{\phi} \qquad (A2)$$

where:

$$k(z) = k_D(z/D)^n, \qquad (A3)$$

is the vertical variation in lateral saturated hydraulic conductivity, n is a constant, and $k_D = k(D)$ (the valid domain of n is discussed in Section 4.2). Solutions to $(A1)$ and $(A3)$ take the form $h(x,t)$ and are expressed (via integration) as discharge flux at the downslope channel per unit width of aquifer: $q(t) = f(a,b,q_0)$, where q_0 is discharge at the onset of recession and catchment outlet discharge is $Q(t) = 2qL$ where L is the length of all upstream channels. Head at the downslope channel is h_0.

Two families of solutions to $(A1)$–$(A3)$ are considered (Table A1), one for flat aquifers (Rupp & Selker, 2005) and one for sloped aquifers (Rupp & Selker, 2006b) (hereafter RS05 and RS06). Exact solutions have been obtained for $h_0 = 0$ and approximations for $0 < h_0 \leq D$. As mentioned in Section 3, we use the collated solutions in Figure 2 and Figure 3 from RS06 as the basis for our generalization, and express (3) in terms of (17) for the case $c_2 = 0$. Beginning with the flat-aquifer late-time analytical solution to (A2) from RS05:

$$-\frac{\mathrm{d}Q}{\mathrm{d}t} = (c_1 D^{-\frac{n}{n+2}}) Q^{\frac{2n+3}{n+2}}, \tag{A4}$$

we write this as:

$$-\frac{\mathrm{d}Q}{\mathrm{d}t} = c_1 D^N Q^b, \tag{A5}$$

which implies $N = 3 - 2b$, and:

$$\frac{\mathrm{d}\bar{\eta}}{\mathrm{d}t} = \frac{\tau}{\phi}\left(\frac{1}{4-2b}\right)\frac{\mathrm{d}\bar{Q}}{\mathrm{d}t}. \tag{A6}$$

This equation can be regarded as a general solution to (20), just as (A4) can be regarded as a general solution to (A2), in the sense that any value of $1 < b < 2$ obtained from recession analysis can be interpreted in terms of n via (A3). This does not imply all values of b have a physically meaningful interpretation (Section 4.2).

We now ask if (A5)–(A6) generalize to flat-aquifer solutions having a constant $k(z)$ profile, as suggested in Section 3 via (17)–(18). Although this question can be answered by simple inspection of $a(D)$ for each of the six early-time solutions and noting that $N = 3 - 2b$ holds in each case, stepping through them provides an opportunity to express (20) in terms of (A6) for each particular value of b, and is useful when we move to the sloped-aquifer case. For constant $k(z)$, $n = 0$, which implies $b = 3/2$, which (as derived in RS05) is consistent with the known nonlinear late-time exact solution for flat, homogeneous aquifers (Boussinesq, 1904). For that solution, $a \neq f(D)$, meaning $N = 0$, and (A6) evaluates to:

$$\frac{\mathrm{d}\bar{\eta}}{\mathrm{d}t} = \frac{\tau}{\phi}\frac{\mathrm{d}\bar{Q}}{\mathrm{d}t} \tag{A7}$$

817 which is consistent with (18) for $\partial_D a = 0$ and with (A6) for $N = 3 - 2b$, given $b = 3/2$.
818 Applied to the linearized late-time solution for homogeneous flat aquifers (Boussinesq, 1903),
819 we have $b = 1$, $N = 1$, and:

820 $$\frac{\mathrm{d}\bar{\eta}}{\mathrm{d}t} = \frac{\tau}{2\phi}\frac{\mathrm{d}\bar{Q}}{\mathrm{d}t} \tag{A8}$$

821 which is consistent with (18) for $\partial_D a = a/D$ and with (A6) for $N = 3 - 2b$, given $b = 1$.
822 Equation (A8) recovers Equation 10 of Brutsaert and Hiyama (2012), also derived from the
823 Boussinesq (1903) linearized solution. A similar substitution of $N = 1$ into (22) recovers
824 Equation 13 of Brutsaert and Hiyama (2012), which can be expressed in terms of b for $N = 3 -$
825 $2b$ as:

826 $$\frac{\mathrm{d}\bar{\eta}}{\mathrm{d}t} = \frac{\eta}{a}\left(\frac{1}{3-2b}\right)\frac{\mathrm{d}a}{\mathrm{d}t}. \tag{A9}$$

827 Although our interest is in late-time solutions, a similar exercise verifies that (A4)–(A6)
828 are internally consistent for the three known early-time ($b = 3$) solutions, one of which is exact,
829 but assumes $h_0 = 0$ and infinite aquifer width (Polubarinova-Kochina, 1962). Specifically, if
830 $b = 3$, then $N = -3$, and (A6) evaluates to $\mathrm{d}\bar{\eta}/\mathrm{d}t = -(2\tau/\phi)\mathrm{d}\bar{Q}/\mathrm{d}t$. This does not prove, but
831 rather demonstrates, as described in Section 3, via (16)–(20), that the definition $b = (2n +$
832 $3)/(n + 2)$ and its relationship to $a(D)$ via $N = 3 - 2b$ generalizes the Brutsaert and Hiyama
833 $\mathrm{d}\bar{\eta}$~$\mathrm{d}\bar{Q}$ analysis to all known functional forms for flat aquifers, or those that can be considered
834 effectively flat.

Table 1: Late-time solutions and parameter definitions in $-\frac{\mathrm{d}Q}{\mathrm{d}t} = c_1 D^N Q^b$ and $\frac{\mathrm{d}\overline{\eta}}{\mathrm{d}t} = \frac{\overline{\tau}}{f}\left(\frac{1}{N+1}\right)\frac{\mathrm{d}\overline{Q}}{\mathrm{d}t}$

Form of Boussinesq equation	b	N $\left(=n(2-b)\right)$	$\frac{\overline{\tau}}{f}\left(\frac{1}{N+1}\right)$	Downstream boundary condition	Reference
linearized	1	$3-2b$	$\frac{\tau}{2f}$	$h_0 = D$	Boussinesq, 1903
non-linear	3/2	$3-2b$	$\frac{\tau}{f}$	$h_0 = 0$	Boussinesq, 1904
non-linear	$\frac{2n+3}{n+2}$	$3-2b$	$\frac{\tau}{2f(2-b)}$	$h_0 = 0$	Rupp & Selker, 2005
linearized	1	$3-2b$	$\frac{\tau}{f}$	$h_0 = D$	Zecharias & Brutsaert, 1988
linearized	1	$3-2b$	$\frac{\tau}{f}$	$h_0 = D$	Sanford, 1993
linearized	1	$3-2b$	$\frac{\tau}{f}$	$h_0 = D$	Sanford, 1993
linearized	1	$3-2b$	$\frac{\tau}{f}$	$h_0 = D$	Steenhuis, 1999
linearized	1	$3-2b$	$\frac{\tau}{f}$	$h_0 = D$	Brutsaert, 1994
non-linear	$\frac{2n+1}{n+1}$	$1-b$	$\frac{\tau}{f(2-b)}$	$h_0 = D$	Rupp & Selker, 2006

A1.2 Sloped aquifers

We first note that a wider variety of solutions exist for sloped aquifers, all of which rely on linearizations of (A2) and assumptions beyond our scope to thoroughly evaluate. As in the previous section, we start with the general solution from RS06 for the $k(z)$ profile given by (A3), in this case for a sloped aquifer:

$$-\frac{\mathrm{d}Q}{\mathrm{d}t} = (c_1 D^{-\frac{n}{n+1}}) Q^{\frac{2n+1}{n+1}} \qquad (A10)$$

which, using the notation $-\mathrm{d}Q/\mathrm{d}t = c_1 D^N Q^b$, implies $N = 1-b$ and therefore:

$$\frac{\mathrm{d}\bar{\eta}}{\mathrm{d}t} = \frac{\tau}{\phi}\left(\frac{1}{2-b}\right)\frac{\mathrm{d}\bar{Q}}{\mathrm{d}t}, \qquad (A11)$$

which departs from (A6) by a factor of two.

As before, we now ask if (A10)–(A11) can be generalized to sloped-aquifer solutions with a constant $k(z)$ profile. Setting aside kinematic wave solutions (e.g., Beven, 1982), six of the 11 sloped-aquifer solutions collated in Figure 3 of RS06 effectively treat $a(D)$ as the horizontal equivalent multiplied by a dimensionless slope factor: $\nu = B/D \tan\theta$. Note that ν represents the balance of gravity-driven flow via $\tan\theta$ versus diffusion via B/D.

In these cases, if ν is treated as a constant parameter, all linearized sloped-aquifer solutions to (A2) conform to $N = 3 - 2b$ and therefore (A6), along with two solutions for which ν is effectively zero. The remaining three solutions include (A10) and two based on (A10), which conform to $N = 1 - b$ and therefore (A11). If ν is not assumed constant, then (18) holds in some cases. Two examples are the late-time $b = 1$ solution of Sanford et al. (1993) and the early-time $b = 3$ solution of Brutsaert (1994) (Table A1).

Equation (A6) and Equation (A11) suggests two families of solutions are applicable. One solution family can be applied to flat (or effectively flat) aquifers, including those with a $k(z)$ profile described by (A3), and to linearized approximations for sloped aquifers with a constant $k(z)$ profile. For these solutions, $N = 3 - 2b$ leads to (A6). The second solution family applies to sloped aquifers with a $k(z)$ profile described by (A3), for which $N = 1 - b$ leads to (A11).

Acknowledgments

The Interdisciplinary Research for Arctic Coastal Environments project funded this work through the United States Department of Energy, Office of Science, Biological and Environmental Research (BER) Regional and Global Model Analysis (RGMA) program areas, under contract grant #89233218CNA000001 to Triad National Security, LLC ("Triad"). The authors have no competing interests, financial or otherwise. Author contributions: MGC designed the study, performed the analysis, prepared the figures, and wrote the manuscript. TZ supervised the project. JCR oversaw funding and project supervision. JS, WRB, and KEB contributed to data curation. All authors contributed to research questions and edited the manuscript.

Data and Software Availability

Data and code required to reproduce all figures in this manuscript are available without restriction from https://github.com/mgcooper/BFRA (Cooper, 2022). The baseflow recession analysis algorithm (v1) is preserved and available without restriction from https://github.com/mgcooper/BFRA. Kuparuk River discharge data are archived at the USGS Water Data for the Nation (https://waterdata.usgs.gov/monitoring-location/15896000/). Rainfall data are archived at the United States National Centers for Environmental Information (https://www.ncdc.noaa.gov/cdo-web/datasets/GHCND/stations/GHCND:USC00505136/detail). MERRA2 climate reanalysis data are archived at the NASA Goddard Earth Sciences and Data Information Services Center (https://disc.gsfc.nasa.gov/datasets?project=MERRA-2). GRACE and GRACE-FO data are archived at the University of Texas at Austin Center for Space Research (http://www2.csr.utexas.edu/grace). Active layer thickness data provided by the Circumpolar Active Layer Monitoring program and the International Permafrost Association are archived at the Arctic Data Center (https://arcticdata.io/catalog/portals/CALM).

References

Aksoy, H., & Wittenberg, H. (2011). Nonlinear baseflow recession analysis in watersheds with intermittent streamflow. *Hydrological Sciences Journal*, *56*(2), 226–237. https://doi.org/10.1080/02626667.2011.553614

Arp, C. D., Whitman, M. S., Kemnitz, R., & Stuefer, S. L. (2020). Evidence of Hydrological Intensification and Regime Change From Northern Alaskan Watershed Runoff. *Geophysical Research Letters*, *47*(17), e2020GL089186. https://doi.org/10.1029/2020GL089186

Aschwanden, M. J. (2015). THRESHOLDED POWER LAW SIZE DISTRIBUTIONS OF INSTABILITIES IN ASTROPHYSICS. *The Astrophysical Journal*, *814*(1), 19. https://doi.org/10.1088/0004-637X/814/1/19

Berghuijs, W. R., Hartmann, A., & Woods, R. A. (2016). Streamflow sensitivity to water storage changes across Europe. *Geophysical Research Letters*, *43*(5), 1980–1987. https://doi.org/10.1002/2016GL067927

Beven, K. (1982). On subsurface stormflow: Predictions with simple kinematic theory for saturated and unsaturated flows. *Water Resources Research*, *18*(6), 1627–1633. https://doi.org/10.1029/WR018i006p01627

Biswal, B., & Kumar, D. N. (2014). Study of dynamic behaviour of recession curves. *Hydrological Processes*, *28*(3), 784–792. https://doi.org/10.1002/hyp.9604

Boussinesq, J. (1903). Sur le débit, en temps de sécheresse, d'une source alimentée par une nappe d'eaux d'infiltration. *CR Hebd. Seanc. Acad. Sci. Paris*, *136*, 1511–1517.

Boussinesq, J. (1904). Recherches théoriques sur l'écoulement des nappes d'eau infiltrées dans le sol et sur le débit des sources. *Journal de Mathématiques Pures et Appliquées*, *10*, 5–78.

Brutsaert, W. (1994). The unit response of groundwater outflow from a hillslope. *Water Resources Research*, *30*(10), 2759–2763. https://doi.org/10.1029/94WR01396

Brutsaert, W. (2005). *Hydrology: An Introduction*. Cambridge: Cambridge University Press. https://doi.org/10.1017/CBO9780511808470

Brutsaert, W. (2008). Long-term groundwater storage trends estimated from streamflow records: Climatic perspective. *Water Resources Research*, *44*(2), W02409. https://doi.org/10.1029/2007WR006518

Brutsaert, W., & Hiyama, T. (2012). The determination of permafrost thawing trends from long-term streamflow measurements with an application in eastern Siberia. *Journal of Geophysical Research: Atmospheres*, *117*(D22). https://doi.org/10.1029/2012JD018344

Brutsaert, W., & Nieber, J. L. (1977). Regionalized drought flow hydrographs from a mature glaciated plateau. *Water Resources Research*, *13*(3), 637–643. https://doi.org/10.1029/WR013i003p00637

Brutsaert, W., & Sugita, M. (2008). Is Mongolia's groundwater increasing or decreasing? The case of the Kherlen River basin / Les eaux souterraines de Mongolie s'accroissent ou décroissent-elles? Cas du bassin versant la Rivière Kherlen. *Hydrological Sciences Journal*, *53*(6), 1221–1229. https://doi.org/10.1623/hysj.53.6.1221

Cheng, L., Zhang, L., & Brutsaert, W. (2016). Automated Selection of Pure Base Flows from Regular Daily Streamflow Data: Objective Algorithm. *Journal of Hydrologic Engineering*, *21*(11), 06016008. https://doi.org/10.1061/(ASCE)HE.1943-5584.0001427

Clauset, A., Shalizi, C. R., & Newman, M. E. J. (2009). Power-Law Distributions in Empirical Data. *SIAM Review*, *51*(4), 661–703. https://doi.org/10.1137/070710111

Cooper, M. G. (2022). Baseflow recession analysis (BFRA) (Version 1). Richland, WA: Pacific Northwest National Laboratory. Retrieved from https://github.com/mgcooper/BFRA

Cooper, M. G., Schaperow, J. R., Cooley, S. W., Alam, S., Smith, L. C., & Lettenmaier, D. P. (2018). Climate Elasticity of Low Flows in the Maritime Western U.S. Mountains. *Water Resources Research*, *54*(8), 5602–5619. https://doi.org/10.1029/2018WR022816

Daly, E., & Porporato, A. (2004). A note on groundwater flow along a hillslope. *Water Resources Research*, *40*(1). https://doi.org/10.1029/2003WR002438

933 Dralle, D. N., Karst, N. J., Charalampous, K., Veenstra, A., & Thompson, S. E. (2017). Event-scale power law
934 recession analysis: quantifying methodological uncertainty. *Hydrology and Earth System Sciences*, *21*(1),
935 65–81. https://doi.org/10.5194/hess-21-65-2017

936 Duan, L., Man, X., Kurylyk, B. L., & Cai, T. (2017). Increasing Winter Baseflow in Response to Permafrost Thaw
937 and Precipitation Regime Shifts in Northeastern China. *Water*, *9*(1). https://doi.org/10.3390/w9010025

938 Earth Resources Observation And Science (EROS) Center. (2018). Interferometric Synthetic Aperture Radar
939 (IFSAR) Alaska [Data set]. U.S. Geological Survey. https://doi.org/10.5066/P9C064CO

940 Evans, S. G., Yokeley, B., Stephens, C., & Brewer, B. (2020). Potential mechanistic causes of increased baseflow
941 across northern Eurasia catchments underlain by permafrost. *Hydrological Processes*, *34*(11), 2676–2690.
942 https://doi.org/10.1002/hyp.13759

943 Feng, D., Gleason, C. J., Lin, P., Yang, X., Pan, M., & Ishitsuka, Y. (2021). Recent changes to Arctic river
944 discharge. *Nature Communications*, *12*(1), 6917. https://doi.org/10.1038/s41467-021-27228-1

945 GDAL/OGR contributors. (2022). *GDAL/OGR Geospatial Data Abstraction software Library*. Open Source
946 Geospatial Foundation. https://doi.org/10.5281/zenodo.5884351

947 Gelaro, R., McCarty, W., Suárez, M. J., Todling, R., Molod, A., Takacs, L., et al. (2017). The Modern-Era
948 Retrospective Analysis for Research and Applications, Version 2 (MERRA-2). *Journal of Climate*, *30*(14),
949 5419–5454. https://doi.org/10.1175/JCLI-D-16-0758.1

950 van de Giesen, N., Steenhuis, T. S., & Parlange, J.-Y. (2005). Short- and long-time behavior of aquifer drainage
951 after slow and sudden recharge according to the linearized Laplace equation. *Advances in Water Resources*,
952 *28*(10), 1122–1132. https://doi.org/10.1016/j.advwatres.2004.12.002

953 Hanel, R., Corominas-Murtra, B., Liu, B., & Thurner, S. (2017). Fitting power-laws in empirical data with
954 estimators that work for all exponents. *PLOS ONE*, *12*(2), e0170920.
955 https://doi.org/10.1371/journal.pone.0170920

956 Hinzman, A. M., Sjöberg, Y., Lyon, S. W., Ploum, S. W., & van der Velde, Y. (2020). Increasing non-linearity of
957 the storage-discharge relationship in sub-Arctic catchments. *Hydrological Processes*, *34*(19), 3894–3909.
958 https://doi.org/10.1002/hyp.13860

959 Hunt, A. G., & Ewing, R. P. (2009). *Percolation theory for flow in porous media* (2nd ed). Berlin: Springer.

960 Huryn, A. D., Gooseff, M. N., Hendrickson, P. J., Briggs, M. A., Tape, K. D., & Terry, N. C. (2021). Aufeis fields
961 as novel groundwater-dependent ecosystems in the arctic cryosphere. *Limnology and Oceanography*, *66*(3),
962 607–624. https://doi.org/10.1002/lno.11626

963 Jachens, E. R., Rupp, D. E., Roques, C., & Selker, J. S. (2020). Recession analysis revisited: impacts of climate on
964 parameter estimation. *Hydrol. Earth Syst. Sci.*, *24*(3), 1159–1170. https://doi.org/10.5194/hess-24-1159-
965 2020

966 Jacques, J.-M. S., & Sauchyn, D. J. (2009). Increasing winter baseflow and mean annual streamflow from possible
967 permafrost thawing in the Northwest Territories, Canada. *Geophysical Research Letters*, *36*(1).
968 https://doi.org/10.1029/2008GL035822

969 Kane, D., Hinzman, L., Stuefer, S., & Arp, C. (2021). Updated Meteorological, Radiation, and Soil Temperature
970 Data, Kuparuk River and Nearby Watersheds: Imnavait B site (IB), 1986-2018. [Text/xml]. NSF Arctic
971 Data Center. https://doi.org/10.18739/A2TQ5RF72

972 Kirchner, J. W. (2009). Catchments as simple dynamical systems: Catchment characterization, rainfall-runoff
973 modeling, and doing hydrology backward. *Water Resources Research*, *45*(2).
974 https://doi.org/10.1029/2008WR006912

975 Kurylyk, B. L., MacQuarrie, K. T. B., & McKenzie, J. M. (2014). Climate change impacts on groundwater and soil
976 temperatures in cold and temperate regions: Implications, mathematical theory, and emerging simulation
977 tools. *Earth-Science Reviews*, *138*, 313–334. https://doi.org/10.1016/j.earscirev.2014.06.006

Liang, X., Zhan, H., Zhang, Y.-K., & Schilling, K. (2017). Base flow recession from unsaturated-saturated porous media considering lateral unsaturated discharge and aquifer compressibility. *Water Resources Research*, *53*(9), 7832–7852. https://doi.org/10.1002/2017WR020938

Liljedahl, A. K., Boike, J., Daanen, R. P., Fedorov, A. N., Frost, G. V., Grosse, G., et al. (2016). Pan-Arctic ice-wedge degradation in warming permafrost and its influence on tundra hydrology. *Nature Geoscience*, *9*(4), 312–318. https://doi.org/10.1038/ngeo2674

Luo, D., Wu, Q., Jin, H., Marchenko, S. S., Lü, L., & Gao, S. (2016). Recent changes in the active layer thickness across the northern hemisphere. *Environmental Earth Sciences*, *75*(7), 555. https://doi.org/10.1007/s12665-015-5229-2

Lv, M., Xu, Z., Yang, Z.-L., Lu, H., & Lv, M. (2021). A Comprehensive Review of Specific Yield in Land Surface and Groundwater Studies. *Journal of Advances in Modeling Earth Systems*, *13*(2), e2020MS002270. https://doi.org/10.1029/2020MS002270

Lyon, S. W., & Destouni, G. (2010). Changes in Catchment-Scale Recession Flow Properties in Response to Permafrost Thawing in the Yukon River Basin. *International Journal of Climatology*, *30*(14), 2138–2145. https://doi.org/10.1002/joc.1993

Lyon, S. W., Destouni, G., Giesler, R., Humborg, C., Mörth, M., Seibert, J., et al. (2009). Estimation of permafrost thawing rates in a sub-arctic catchment using recession flow analysis. *Hydrol. Earth Syst. Sci.*, *13*(5), 595–604. https://doi.org/10.5194/hess-13-595-2009

McKenzie, J. M., Kurylyk, B. L., Walvoord, M. A., Bense, V. F., Fortier, D., Spence, C., & Grenier, C. (2021). Invited perspective: What lies beneath a changing Arctic? *The Cryosphere*, *15*(1), 479–484. https://doi.org/10.5194/tc-15-479-2021

McMillan, H. (2020). Linking hydrologic signatures to hydrologic processes: A review. *Hydrological Processes*, *34*(6), 1393–1409. https://doi.org/10.1002/hyp.13632

McNamara, J. P., Kane, D. L., & Hinzman, L. D. (1998). An analysis of streamflow hydrology in the Kuparuk River Basin, Arctic Alaska: a nested watershed approach. *Journal of Hydrology*, *206*(1), 39–57. https://doi.org/10.1016/S0022-1694(98)00083-3

Nyland, K. E., Shiklomanov, N. I., Streletskiy, D. A., Nelson, F. E., Klene, A. E., & Kholodov, A. L. (2021). Long-term Circumpolar Active Layer Monitoring (CALM) program observations in Northern Alaskan tundra. *Polar Geography*, *44*(3), 167–185. https://doi.org/10.1080/1088937X.2021.1988000

O'Connor, M. T., Cardenas, M. B., Neilson, B. T., Nicholaides, K. D., & Kling, G. W. (2019). Active Layer Groundwater Flow: The Interrelated Effects of Stratigraphy, Thaw, and Topography. *Water Resources Research*, *55*(8), 6555–6576. https://doi.org/10.1029/2018WR024636

Polubarinova-Kochina, P. I. (1962). *Theory of ground water movement*. Princeton, N.J.: Princeton University Press.

Rantz, S. E. (1982). *Measurement and computation of streamflow: Volume 1. Measurement of Stage and Discharge* (USGS Numbered Series No. 2175). *Measurement and computation of streamflow* (Vol. 2175). U.S. G.P.O. https://doi.org/10.3133/wsp2175

Rawlins, M. A., Cai, L., Stuefer, S. L., & Nicolsky, D. (2019). Changing characteristics of runoff and freshwater export from watersheds draining northern Alaska. *The Cryosphere*, *13*(12), 3337–3352. https://doi.org/10.5194/tc-13-3337-2019

Rennermalm, A. K., Wood, E. F., & Troy, T. J. (2010). Observed changes in pan-arctic cold-season minimum monthly river discharge. *Climate Dynamics*, *35*(6), 923–939. https://doi.org/10.1007/s00382-009-0730-5

Roques, C., Rupp, D. E., & Selker, J. S. (2017). Improved streamflow recession parameter estimation with attention to calculation of − dQ/dt. *Advances in Water Resources*, *108*, 29–43. https://doi.org/10.1016/j.advwatres.2017.07.013

Rowland, J. C., Travis, B. J., & Wilson, C. J. (2011). The role of advective heat transport in talik development beneath lakes and ponds in discontinuous permafrost. *Geophysical Research Letters*, *38*(17). https://doi.org/10.1029/2011GL048497

Rupp, D. E., & Selker, J. S. (2005). Drainage of a horizontal Boussinesq aquifer with a power law hydraulic conductivity profile. *Water Resources Research*, *41*(11), W11422. https://doi.org/10.1029/2005WR004241

Rupp, D. E., & Selker, J. S. (2006a). Information, artifacts, and noise in dQ/dt − Q recession analysis. *Advances in Water Resources*, *29*(2), 154–160. https://doi.org/10.1016/j.advwatres.2005.03.019

Rupp, D. E., & Selker, J. S. (2006b). On the use of the Boussinesq equation for interpreting recession hydrographs from sloping aquifers. *Water Resources Research*, *42*(12), W12421. https://doi.org/10.1029/2006WR005080

Rupp, D. E., Schmidt, J., Woods, R. A., & Bidwell, V. J. (2009). Analytical assessment and parameter estimation of a low-dimensional groundwater model. *Journal of Hydrology*, *377*(1–2), 143–154. https://doi.org/10.1016/j.jhydrol.2009.08.018

Sanford, W. E., Parlange, J.-Y., & Steenhuis, T. S. (1993). Hillslope drainage with sudden drawdown: Closed form solution and laboratory experiments. *Water Resources Research*, *29*(7), 2313–2321. https://doi.org/10.1029/93WR00515

Save, H., Bettadpur, S., & Tapley, B. D. (2016). High-resolution CSR GRACE RL05 mascons. *Journal of Geophysical Research: Solid Earth*, *121*(10), 7547–7569. https://doi.org/10.1002/2016JB013007

Sergeant, F., Therrien, R., Oudin, L., Jost, A., & Anctil, F. (2021). Evolution of Arctic rivers recession flow: Global assessment and data-based attribution analysis. *Journal of Hydrology*, *601*, 126577. https://doi.org/10.1016/j.jhydrol.2021.126577

Sjöberg, Y., Jan, A., Painter, S. L., Coon, E. T., Carey, M. P., O'Donnell, J. A., & Koch, J. C. (2021). Permafrost Promotes Shallow Groundwater Flow and Warmer Headwater Streams. *Water Resources Research*, *57*(2), e2020WR027463. https://doi.org/10.1029/2020WR027463

Smith, L. C., Pavelsky, T. M., MacDonald, G. M., Shiklomanov, A. I., & Lammers, R. B. (2007). Rising minimum daily flows in northern Eurasian rivers: A growing influence of groundwater in the high-latitude hydrologic cycle. *Journal of Geophysical Research: Biogeosciences*, *112*(G4). https://doi.org/10.1029/2006JG000327

Szilagyi, J., Gribovszki, Z., & Kalicz, P. (2007). Estimation of catchment-scale evapotranspiration from baseflow recession data: Numerical model and practical application results. *Journal of Hydrology*, *336*(1), 206–217. https://doi.org/10.1016/j.jhydrol.2007.01.004

Taylor, B. N., & Kuyatt, C. E. (1994). *Guidelines for Evaluating and Expressing the Uncertainty of NIST Measurement Results (NIST Technical Note vol 1297)* (p. 24). Gaithersburg, MD: National Institue of Standards and Technology. Retrieved from http://physics.nist.gov/Pubs/guidelines/TN1297/tn1297s.pdf

Troch, P. A., Carrillo, G. A., Heidbüchel, I., Rajagopal, S., Switanek, M., Volkmann, T. H. M., & Yaeger, M. (2009). Dealing with Landscape Heterogeneity in Watershed Hydrology: A Review of Recent Progress toward New Hydrological Theory. *Geography Compass*, *3*(1), 375–392. https://doi.org/10.1111/j.1749-8198.2008.00186.x

Tsallis, C. (1988). Possible generalization of Boltzmann-Gibbs statistics. *Journal of Statistical Physics*, *52*(1), 479–487. https://doi.org/10.1007/BF01016429

Walvoord, M. A., & Kurylyk, B. L. (2016). Hydrologic Impacts of Thawing Permafrost-A Review. *Vadose Zone Journal*, *15*(6), vzj2016.01.0010. https://doi.org/10.2136/vzj2016.01.0010

Walvoord, M. A., & Striegl, R. G. (2007). Increased groundwater to stream discharge from permafrost thawing in the Yukon River basin: Potential impacts on lateral export of carbon and nitrogen. *Geophysical Research Letters*, *34*(12). https://doi.org/10.1029/2007GL030216

Walvoord, M. A., Voss, C. I., & Wellman, T. P. (2012). Influence of permafrost distribution on groundwater flow in the context of climate-driven permafrost thaw: Example from Yukon Flats Basin, Alaska, United States. *Water Resources Research*, *48*(7). https://doi.org/10.1029/2011WR011595

Yang, D., Kane, D., Zhang, Z., Legates, D., & Goodison, B. (2005). Bias corrections of long-term (1973–2004) daily precipitation data over the northern regions. *Geophysical Research Letters*, *32*(19). https://doi.org/10.1029/2005GL024057

Yi, S., & Sneeuw, N. (2021). Filling the Data Gaps Within GRACE Missions Using Singular Spectrum Analysis. *Journal of Geophysical Research: Solid Earth*, *126*(5), e2020JB021227. https://doi.org/10.1029/2020JB021227

York, D., Evensen, N. M., Martínez, M. L., & De Basabe Delgado, J. (2004). Unified equations for the slope, intercept, and standard errors of the best straight line. *American Journal of Physics*, *72*(3), 367–375. https://doi.org/10.1119/1.1632486

Zecharias, Y. B., & Brutsaert, W. (1988a). Recession characteristics of groundwater outflow and base flow from mountainous watersheds. *Water Resources Research*, *24*(10), 1651–1658. https://doi.org/10.1029/WR024i010p01651

Zecharias, Y. B., & Brutsaert, W. (1988b). The influence of basin morphology on groundwater outflow. *Water Resources Research*, *24*(10), 1645–1650. https://doi.org/10.1029/WR024i010p01645